Three-dimensional measurement of the crater formation during plume-surface interactions using stereo-photogrammetry

DC Stubbs[*], L Silwal[†], BS Thurow[‡], M Hirabayashi[§], V Raghav[¶], and DE Scarborough[‖]

Department of Aerospace Engineering, Auburn University, Auburn, Alabama, 36849

The present investigation focused on adapting and validating stereo-photogrammetry for obtaining 3-D, time-resolved, non-intrusive, full-domain measurements of crater evolution during the plume-surface interaction (PSI) process. An atmospheric experimental facility was designed and constructed to facilitate the development of the stereo-photogrammetry technique for PSI applications. Stereo-photogrammetry was then used to measure the dynamic crater evolution process at nozzle heights of 25, 40, 55, and 70 nozzle diameters above the sand simulant bed. From the stereo-photogrammetry data, time-resolved 3-D reconstructions of the crater geometry were generated, and crater depth, radius, and volume time histories were extracted. Crater depth was observed to grow logarithmically for the two highest nozzle heights, and the depth growth rate for the lower two nozzle heights was more rapid. Crater volume growth was well characterized by a power law fit. The slope of the collapsed crater post nozzle flow was found to increase with nozzle height, along with the final crater volume. The results show that stereo-photogrammetry can be used to successfully measure the crater geometry in cases where optical access to the crater is not completely degraded by ejected particles.

Nomenclature

D	=	nozzle diameter
d	=	array of depth values for each point in the crater
h	=	height of nozzle above lunar simulant
N	=	total number of points in the point cloud
n_p	=	number of points in nearest neighbor average
n_s	=	number of experimental runs
n_x	=	number of depth grid points in the x direction
n_y	=	number of depth grid points in the y direction
S	=	surface area of the simulant bed
t	=	time
V	=	volume of the crater
X	=	magnitude of the distance between two points
$\overline{X}$	=	mean distance from a particle to its n_p – nearest neighbors
μ_d	=	mean crater depth
μ_r	=	mean crater radius
μ_V	=	mean crater volume
ρ	=	bulk density of sand
σ_d	=	standard deviation of mean crater depth
σ_r	=	standard deviation of mean crater radius
σ_V	=	standard deviation of mean crater volume
σ_χ	=	standard deviation of the overall mean distance to n-nearest neighbors
χ	=	overall mean distance to n-nearest neighbors

[*]Graduate Research Assistant, Aerospace Engineering, AIAA Student Member
[†]Graduate Research Assistant, Aerospace Engineering, AIAA Student Member
[‡]Professor and Department Chair, Aerospace Engineering, AIAA Member
[§]Assistant Professor, Aerospace Engineering, AIAA Member
[¶]Assistant Professor, Aerospace Engineering, AIAA Member
[‖]Assistant Professor, Aerospace Engineering, AIAA Member

I. Introduction

In the next decade, NASA is prioritizing returning humans safely to the Moon via the Artemis program, deploying scientific instruments on a variety of extraterrestrial bodies, and ultimately enabling human exploration of Mars. One key issue to achieving these objectives is adequately understanding the Plume-Surface Interaction (PSI) process. The PSI process is the process wherein an exhaust plume from a rocket interacts with the surface of some planetary body or asteroid during descent or liftoff. When rocket exhaust impinges on a planetary surface covered by regolith, fragmented layers containing loose granular materials, the surface materials begin to erode away forming a crater. As part of this crater formation process, the material can be ejected from the crater at very high velocities that creates a dust cloud and presents a hazard to nearby scientific instruments that may already be on the surface. Complications arising from the the interaction between spacecraft and PSI have already been observed in a microgravity environment. The effects of the PSI ejecta cloud were noted during the Apollo 12 mission where the Surveyor III craft was found to have experienced surface pitting as a result of being exposed only to the fringes of the ejecta cloud [1].

The PSI process becomes especially significant when larger landers with more thrust, such as the ones needed to enable manned missions, are used [2]. Astronauts John Young and Gene Cernan considered lunar dust to be among the most important obstacles to returning to and operating on the moon [3, 4]. Due to the potential for damage to surrounding hardware by the blowing dust and debris, it is important to understand the interaction between the lander's exhaust plume and the lunar regolith. The evolution of the regolith surface topography during retrorocket firing is important to understanding surface particle ejection into the surface flow. Particles moved along the regolith surface by the jet encounter these variations in the surface topography and can be launched upward and entrained into the surface flow. Metzger et al. noted that neither mass erosion rate nor ejection angles have been adequately determined [2].

Obtaining full-scale experimental data for this problem is challenging given the difficulties in conducting full-scale experiments on earth that accurately replicate the near-vacuum lunar atmosphere and the lunar gravity. Additionally, there is a lack of any truly analogous sites on earth that replicate the lunar regolith conditions [5]. Because of the difficulties in conducting realistic, full-scale experiments on earth, computer simulations are required to predict the interaction between the nozzle flow field and the lunar regolith, which results in a complex two-phase flow field. Until recent years, this too, has been nearly impossible due to the lack of computational power and a lack of understanding of the underlying physics of the problem. However, in recent years computational power has improved to the point of making accurate simulations possible. Unfortunately, the underlying physics involved in the PSI process are still not understood well enough to develop accurate models [5, 6].

While significant seminal work focused on identifying many of the important physical parameters governing PSI, these previous investigations were mostly conducted in flow-intrusive, partial-domain experiments (Section II). Therefore, the need exists to conduct full-domain experimental investigations utilizing non-intrusive diagnostics. The goal of this study was to address this need by adapting and maturing stereo-photogrammetry to enable 3-D, time-resolved measurements of the crater formation process during plume-surface interactions in a full-domain experiment. This paper, which details this effort, is organized as follows. First, some background on crater formation mechanisms and previously used measurement techniques is presented. Next, we describe the experimental plume-surface interaction facility, which was tailored to allow for the use of stereo-photogrammetry. Third, the stereo-photogrammetry procedure and associated algorithms for extracting crater depth, radius, and volume from the 3-D crater reconstructions are described. This is followed by a presentation of an experimental study of the accuracy of the stereo-photogrammetry technique adapted for this study. Finally, measurements of the 3-D, dynamic crater evolution process are presented and compared with results from previous works.

II. Background

Research into crater formation resulting from plume-surface interactions initially started in the 1960's due to its relevance to landing on the Moon during the Apollo program. Eastman et al. [7] studied the flow field of an exhaust plume impinging on a simulated lunar surface to determine the lunar surface pressure for various nozzle heights above the lunar surface. Plesik et al. [8] measured heat transfer and surface pressure distribution on a surface under high-vacuum conditions. Clark [9] conducted a series of tests using a model of the lunar module retrorocket in a vacuum chamber. The retrorocket exhaust flow of the model was impinged onto flat and dished plates instrumented with pressure transducers and calorimeters to measure the target-surface impingement pressures and heating rates with the test rocket at various altitudes and attitudes above the surface, and at multiple thrust levels [9]. These initial studies helped with the development and understanding of the crater formation process, but did not measure the crater formation directly.

To measure the actual crater formation, a subsequent study conducted by Land and Connor [10] utilized an X-ray imaging technique to measure crater growth. In this technique a bed of lunar simulant was placed on a plate and an X-ray source was located above the simulant bed. A slit was cut in the plate to allow the X-rays to pass and film was moved across the slot at a constant speed to measure the amount of X-rays passing through. In this way, the intensity of the measured X-rays was calibrated to a corresponding thickness of the lunar simulant and the crater formation was measured over time. While this early study measured the time history of the crater formation, many initial works studying crater formation typically focused on the asymptotic crater size [11, 12]. For instance, Rajaratnam and Mazurek observed impingement at a number of time intervals until an end or asymptotic state was reached; in the remainder of the experiments, only the erosion profile at asymptotic state was measured [13].

More modern studies have leveraged the capabilities of optical diagnostics to measure the crater formation process. Clark and Behringer used a thin box to simulate a 2-D crater formation [14]. This 2-D experimental domain was used to facilitate optical access to a cross-section of the crater profile. A camera was used to take images of the crater cross-section at 100 Hz from which the crater depth, shape, and the horizontal position of the bottom of the crater were measured. Badr et al. used a laser profilometer to measure crater depth along a 2-D line extending from the center of the crater radially outwards to the edge of the crater [15]. While the crater was 3-D, this measurement technique only measured depth along a 2-D line. Additionally, this technique was only used to measure the steady crater shapes that result once the crater has reached its asymptotic state.

Perhaps the most commonly used experimental setup in recent years involves the use of a transparent plate having a beveled edge aligned with the symmetry plane of the nozzle flow to split the nozzle flow and allow optical access to a cross-section of the crater [16–22]. A camera is typically pointed at the transparent splitter plate to optically measure the crater profile at the cross-section. Using this technique, the crater depth, radius, volume, and erosion rate have been studied. This technique appears to have first been used by Haehnel et al. to study the crater formation of subsonic jets in three different beds of granular materials [16]. Haehnel et al. conducted experiments at both fixed and descending nozzle heights with a 2.5 cm diameter nozzle having an exit velocity of 100 m/s [16]. In a subsequent study, Haehnel et al. studied the impact of the permeability of the bed material on the crater formation and also provided an empirical method for predicting the slope and depth of the crater as a function of jet strength [17]. Metzger et al. [18, 23] expanded upon the work by Haehnel et al. by taking crater formation measurements in a sand bed under Earth atmospheric conditions with jet velocities ranging from $37 - 56 \, m/s$ using five different gases (helium, neon, nitrogen, argon, and carbon dioxide) to study the impact of jet gas density on the crater formation process [18]. In this study, the optical techniques were unable to be used at higher jet-velocities due to the turbulent fluidiziation of the material making optical measurements prohibitively difficult. In a separate study, Immer and Metzger adapted the splitter plate experimental setup for use in reduced gravity flights to measure the crater formation in simulated Lunar and Martian gravity [19]. LaMarche et al. [21] have used the same experimental setup as Metzger et al. [18] to study the erosion rate of craters in JSC-1A Lunar simulant. Later, LaMarche and Curtis [22] used the split plate technique to study the effect of particle shape on the crater evolution process. Most recently, the split plate technique has been used by Guleria et al. [20] to study the formation of craters in millimeter scale glass beads compared to the micrometer scale particles studied by Metzger et al.

In a similar idea to the split plate technique, Mehta et al. created a quarter space technique to study the effect of exhaust impingement from a pair of 25% scale Viking lander engines onto Martian simulant in a test chamber maintained at Martian atmospheric pressure [24]. In this quarter space technique, two clear baffle plates were positioned at 90° on either side of the engine to simulate the neighboring thruster plumes, representing a nominal configuration of four engines interacting with each other. A high-speed camera operating at 500 frames per second was positioned to measure the crater forming through the baffle plates at the impingement site to capture the erosion dynamics. Post-test measurement of eroded depth and diameter were used to determine the instantaneous and average erosion rate. This same experimental setup was used to study the interaction of subscale Phoenix engine nozzles with a granular bed of Martian simulant in a subsequent study by Mehta et al. [25].

In cases where optical access to the crater was prevented due to rapid fluidization of the sand bed, or when the desire is to study the flow of particles under the surface, layers of colored sand have been used to provide insight into the crater formation process. Metzger et al. [18, 23] used this technique by creating a sand bed out of thin horizontal layers of colored sand. The sand was cratered by a jet, the jet was extinguished, and the collapsed crater was filled with epoxy to preserve its shape. Lastly, the epoxy layers were hardened such that a cross-section could be cut away to analyze how the initially horizontal layers of sand had deformed beneath the surface as a result of the cratering process.

In addition to measuring the crater evolution during PSI, previous studies have, so far, identified four mechanisms of crater formation during PSI. These mechanisms are: viscous erosion, bearing capacity failure, diffused gas eruption,

and diffusion-driven flow, briefly described below.

1) Viscous erosion occurs along the topmost later of regolith when the dynamic pressure on the particles from the jet flow moves the particles radially away from the plume center forming a crater. The theory of viscous erosion was originally developed by Roberts [26–29], was applied to the lunar landings by Hutton [30], and was later modified by Metzger [31] to account for particle ejection angle and soil particle distribution.

2) Bearing capacity failure occurs when the stagnation pressure beneath the jet exceeds the bearing capacity of the soil. In this case, the soil is pushed downward forming a nearly cylindrical crater [32]. In the cases in which bearing capacity failure occurs, it has been found to continue until the crater is just slightly deeper than the length of the jet at which point viscous erosion becomes the dominant mechanism [23].

3) Diffused gas eruption was first described by Scott and Ko [33] who fired rocket motors into soil and observed that radial diffusion of pressure could blow out a toroidal region around the exhaust jet. Pressure beneath the engine diffused radially outward until the pressure was able to lift the overlying soil. They also observed that upon engine shut down, a spike of soil could blow up the center of the engine nozzle.

4) Diffusion-driven flow, also called diffusion-driven shearing, was originally identified as a fourth mechanism for crater formation by Metzger et al. [2, 18]. Diffusion-driven flow is the mechanism in which the drag forces of gas diffusing through the sand creates a large enough body force on the sand to exceed the shear strength of the sand and initiate shearing. This shearing then results in the sand flowing away from the center of the crater in thick bands tangential to the surface of the crater such that the crater continues to deepen. The bands of sand then get moved up the sides of the crater by the shear stress resulting in upward deformation of the sand layers [2].

While results and knowledge generated from these split plate and quarter space techniques are useful, such techniques are intrusive, potentially altering the physics of the crater formation process. This has been pointed out in the studies by Guleria et al. [20] and LaMarche et al. [22], which both highlight that the presence of the split plate is intrusive to the flow profile of the jet and that a boundary layer builds on the window potentially altering the results of the experiment. Additionally, optical diagnostics used to measure the crater in the split plate style experiments have measured the 2-D crater cross-section at the split plate location, and the geometric parameters such as depth and volume have been extracted from these 2-D profiles rather than measuring the 3-D crater geometry directly.

This study contributes to the existing body of research by adapting stereo-photogrammetry to measure the crater formation process. Stereo-photogrammetry involves the use of two cameras with each of them viewing different perspectives of the same object. The corresponding features between the stereo image pair are then matched and the 3-D reconstruction of the object is calculated via triangulation [34]. Stereo-photogrammetry provides the advantage of non-intrusive measurements with subpixel accuracy [35], which has prompted an increase in its use in a myriad of fields such as navigation of autonomous vehicles [36, 37], agriculture [38, 39], and forestry [40]. It has also been used for geographical study of static sand and soil surfaces under different conditions [41–43]. In the present study, stereo-photogrammetry was adapted to measure the dynamic crater formation in a sand bed due to an impinging jet without concern of a split plate adversely affecting the results of the experiment. This measurement is challenging due to degraded optical access resulting from particles ejected from the crater. Therefore, the performance of stereo-photogrammetry under these optically degraded conditions was also explored.

The high-speed cameras used in this study were used to acquire data at a rate of 1,000 Hz. This acquisition rate is higher than many previous works, which have typically acquired data in the range of 10-500 Hz. This high acquisition rate allows for detailed measurement of the crater at times less than 1 s, whereas most previous works have focused on the long-term transient crater growth (on the order of 100 s) [22]. This < 1 s regime is of particular interest for validating multi-phase flow models currently under development for simulating PSIs [22, 44]. While the family of splitter plate techniques used extensively throughout crater formation research has proven useful in a laboratory environment where such an experiment can be constructed, the stereo-photogrammetry technique presented in this paper has the potential to be extended to taking in-situ measurements in the field, and thus could possibly be mounted to space craft in the future for taking full-scale data of the crater formation process.

III. Experimental Facility and Instrumentation

A full-domain atmospheric experimental facility was designed and fabricated with the aim of facilitating non-intrusive, time-resolved, 3-D measurements of the crater geometry evolution during the PSI process. The experimental facility, shown in Fig. 1a, consists of a 1 m long, 1 m wide, and 1 m tall "test section", which was covered by a clear acrylic shield. This acrylic shield placed between the optical diagnostics and the test section prevents camera damage by any ejected simulant particles. The test section is enclosed using clear panels on three sides and an opaque panel on one

side. The clear side panels provide optical access to the simulant bed while the opaque panel provides a background for side-view optical diagnostics. The bottom of the facility was closed to provide a solid, vibration-free floor for the regolith simulant. The structure above the test section was developed to facilitate mounting the stereo camera pair and other diagnostics hardware and is open to the atmosphere.
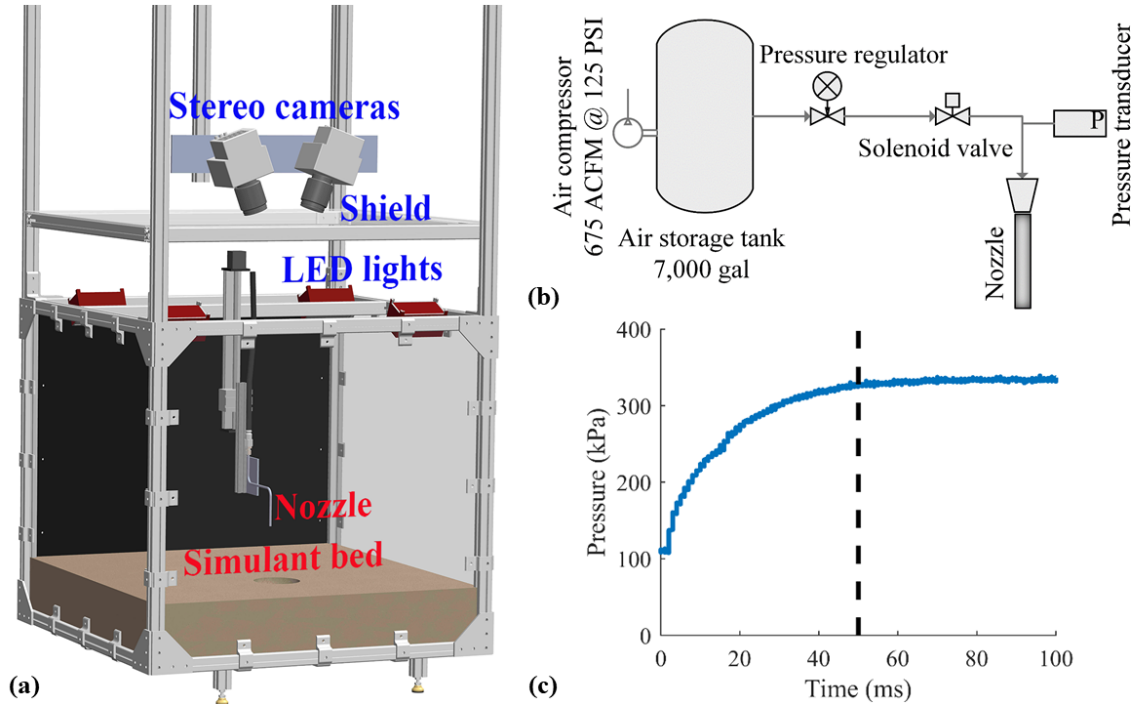

Fig. 1 **(a) Schematic representation of the atmospheric experimental facility for PSI studies; (b) Schematic of nozzle flow system; (c) Pressure transients at the nozzle during startup**

The impinging jet was provided by a constant area nozzle utilizing an aluminum tube with a constant inner diameter of 4.57 mm. This nozzle configuration was chosen as it was simple to manufacture while still providing underexpanded sonic exit flow that could effectively be used to develop the optical diagnostic techniques. Care was taken to ensure the jet was orthogonal to the simulant surface. Further, the nozzle was mounted to a linear translation system to allow for remote nozzle height positioning. While not used for this study, the nozzle translation system also provides the capability to study crater formation during nozzle descent. The nozzle can be positioned at heights ranging from 0 mm to 330 mm above the simulant surface and is capable of descending at rates ranging from 0 mm/s to 50 mm/s.

Compressed air was provided to the nozzle using the nozzle flow system illustrated in Fig. 1b. The air supply pressure was adjusted using a Norgren® R74G-6AT-RMG pressure regulator to obtain an under-expanded choked flow with a Mach number of 1 at the nozzle exit. A Granzow® Inc. H4H29-00Y solenoid valve directly upstream of the nozzle was used to remotely control the start and stop of nozzle flow. An Endevco 8530BM37-200-1 pressure transducer was mounted directly upstream of the nozzle to monitor the static pressure during testing. A sample pressure time history is shown in Fig. 1c. From this figure, we see that nozzle startup transients continue for approximately 50 ms, after which steady flow conditions were achieved for the duration of the experiment. The steady-state nozzle pressure during testing was 322 kPa. The mass flow through the nozzle was measured using an Omega™ FMA5545 mass flow meter to be 0.0085 kg/s. The remaining nozzle flow conditions, tabulated in Table 1, were calculated from these measured values.

Figure 2 consists of a series of schlieren images taken using the background oriented schlieren (BOS) technique [45], which show the flow field during nozzle startup. After approximately 50 ms, supersonic exit flow was established, which is in agreement with the startup pressure transients shown in Fig. 1c. From 50 to 80 ms, supersonic exit flow continues to develop, and by 80 ms the exit flow is fully established. The exit flow was observed to be axisymmetric, stable in the near-field, and slightly oscillating or flapping in the far-field.

Table 1   Flow conditions of the under-expanded nozzle

Property	Value	Method
Inlet static pressure	322 kPa	Measured
Inlet total pressure	355 kPa	Calculated
Nozzle inner diameter	4.57 mm	Measured
Exit Mach Number	1.0	Calculated
Mass flow rate	0.0085 kg/s	Measured
Exit velocity	314 m/s	Calculated
Exit static pressure	110 kPa	Calculated
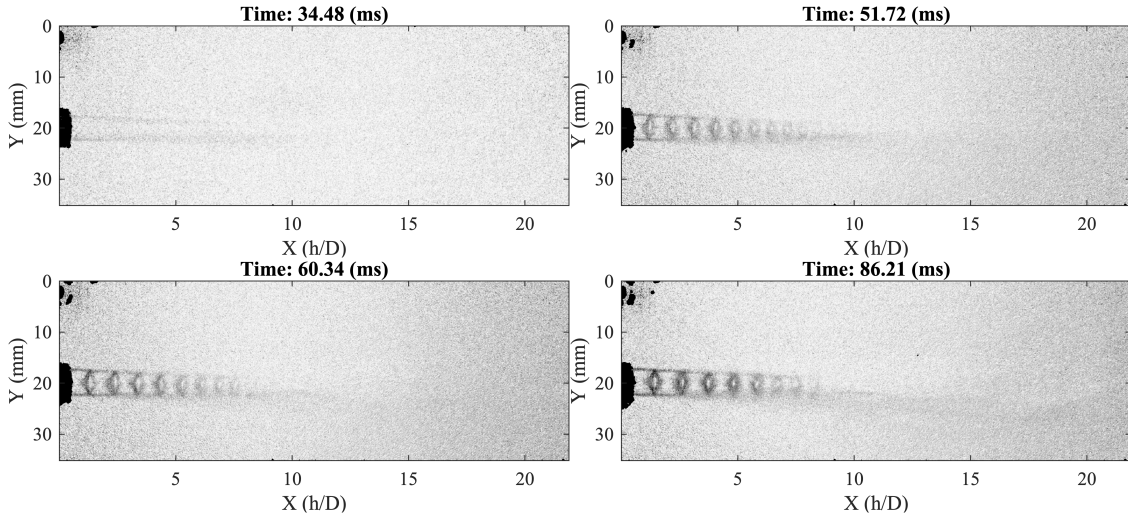
Fig. 2   Schlieren results showing the density gradients of the nozzle exit flow.

High-speed stereo image pairs were obtained using two Phantom® VEO 640L high-speed cameras. These cameras were used to capture images with a resolution of 2560 × 1600 pixels at 1000 frames per second. Two variable focal length lenses with identical specifications were used for each camera and the focal length was set to 70 mm for each lens. This configuration resulted in a spatial resolution of 0.16 $mm/pixel$ at the simulant bed surface. An exposure time of 100 μs was used to reduce blurring caused by rapidly moving particles ejected from the crater. The camera pair was mounted above the test section using a series of t-slotted framing rails and a custom mounting plate to provide precision placement of the cameras in 3-D space. The camera mounting plate had multiple mounting holes with 25.4 mm spacing to provide for adjustment in the lateral spacing between the cameras. The viewing angles of the cameras were measured and set using a digital level. Multiple camera configurations, i.e., lateral spacings and viewing angles, were investigated. The details regarding the exact positioning of the cameras for this work are described in the next section (Sec. IV.A).

High-intensity, stable illumination of the target is required to obtain images at the high-frame rates and low exposure times needed. A set of four GS Vitec QT LED lights, outlined in red in Fig. 1a, were used to illuminate the surface with 48, 000 lm of flicker-free light. The lights were mounted at each corner of the top of the test chamber 635 mm above the simulant surface and "focused" onto the simulant bed using 30° lenses.

The nozzle flow solenoid valve, nozzle linear translation system, and stereo camera pair were controlled remotely via a National Instruments (NI) data acquisition (DAQ) system. The system comprised a NI cDAQ-9189 chassis with a NI 9482 relay module for triggering the cameras and solenoid valve, a NI 9474 digital output module for controlling the stepper motor, and a NI 9205 analog voltage input module for reading the pressure transducer. The DAQ provides the capability to time-synchronize data acquired across the multiple diagnostic techniques.

Sand was selected as the regolith simulant for this work due to it being readily available, inexpensive, and its common use as a simulant in previous studies [2, 14, 18]. Commercially available sieved sand with a particle size range

of 600 to 850 μm was used for all tests. This particle size range was chosen to limit the number of fine particles being ejected from the crater that would impede optical access. The sand was cohesionless, naturally rounded, nearly pure quartz, and conformed to the ASTM C 778 standard with a reported particle density of 2,650 kg/m^3. For each test, the sand was placed in a container 580 mm wide, 580 mm long, and 200 mm deep. The container was completely filled with sand and the surface was leveled using a straight edge to ensure a uniform, undisturbed simulant. The bulk density (ρ) of the sand used was 1650 kg/m^3, which indicates a packing ratio of 0.6.

IV. Stereo-Photogrammetry and Data Processing

For this study, standard stereo-photogrammetry methods were adapted and applied to non-intrusively measure the dynamic crater formation process in the developed full-domain experiment described above. This section details the implemented stereo-photogrammetry technique, as well as, the algorithms used to extract the relevant crater geometric parameters, i.e., crater depth, radius, and volume evolution.

A. Stereo-Photogrammetry

Stereo-photogrammetry is an optical technique wherein the coordinates of an object in 3-D space are measured by taking two or more planar images from different perspectives relative to the object of interest. The process for reconstructing the 3-D scene involves identifying common points on each image, drawing rays from the camera location to the common points on the object being imaged, and finally performing triangulation to determine the intersection of these rays that determines the 3-D locations of these points in world coordinates [34]. A diagram of the stereo-photogrammetry technique is shown in Fig. 3. The first step towards the adaptation of the stereo-photogrammetry technique for the measurement of the crater formation process was to determine the positioning of the cameras relative to the crater such that an optimum view of the crater could be maintained.
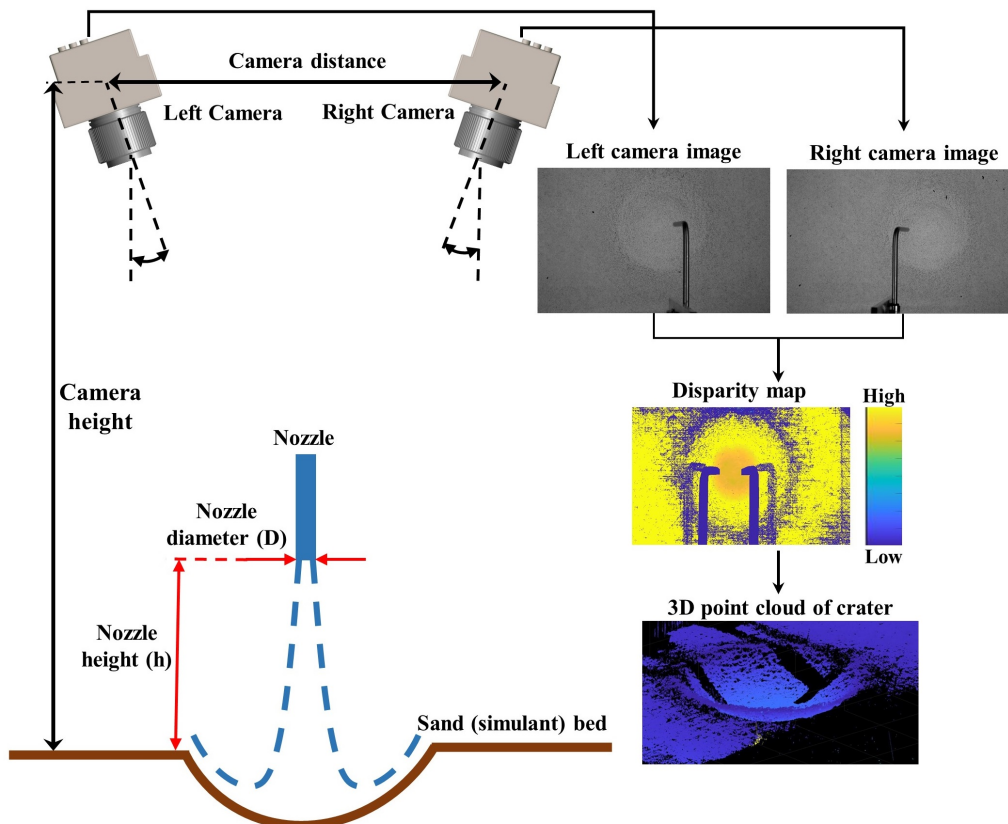

Fig. 3 Diagram depicting the stereo-photogrammetry setup. Original stereo image pair (the raw data) and the resulting disparity map. Point cloud representing the reconstructed crater geometry output from the stereo image processing program.

Three different camera configurations, i.e., parallel, converging, and wide-converging, were investigated as part of this study to determine the optimal configuration for measuring the crater formation process. In the parallel configuration, the lateral spacing between the cameras was 125 *mm* with a viewing angle of 0° as shown in Fig. 3. The spacing of 125 *mm* was the minimum possible lateral spacing achievable due to the physical dimensions of the camera bodies, and therefore represented the maximum possible overlap between the field of view (FOV) of the two cameras. In the "converging" and and "wide-converging" configurations, the lateral spacing of the cameras was increased and the viewing angle of the cameras was adjusted such that the view of both cameras was still centered on the crater. In the case of the converging configuration the lateral spacing between the cameras was 200 *mm* with a viewing angle of 5.9°. For the wide-converging configuration the lateral spacing between the cameras as 400 *mm* with a viewing angle of 12°.

In an ideal stereo camera system the stereo camera pair would be perfectly oriented such that the image planes of the stereo image pair are coplanar [34]. In reality, this will never be the case, and thus the process of *stereo rectification* is used to reproject the image planes of the stereo camera pair so that they reside in the exact same plane [34]. As such, it is generally preferable to mount the stereo camera pair in a parallel configuration such that the degree to which the rectification algorithm must re-project the images is minimized. However, for this work the parallel configuration resulted in increased obstruction of the camera's view of the crater center region from the nozzle compared to the converging configurations. Thus, the converging configuration was used as a compromise. The converging-wide configuration was tested, but it resulted in the images being too far apart on the epipolar plane after rectification, which in turn resulted in the failure of the stereo reconstruction algorithm used due to the high disparity values. This is visualized in Fig. 4, which shows anaglyphs of the rectified stereo image pairs for the parallel, converging, and wide-converging camera configurations.
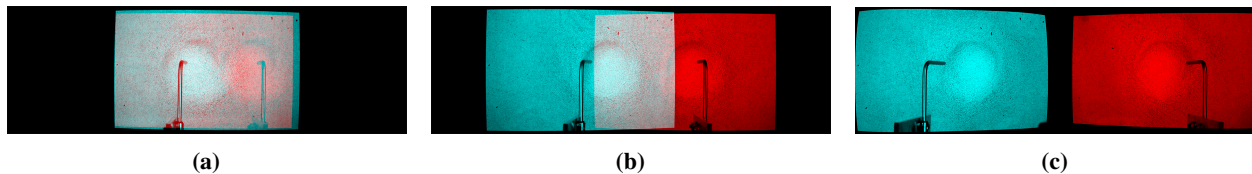

(a) **(b)** **(c)**

Fig. 4 Stereo anaglyphs of the (a) parallel, (b) converging, and (c) wide-converging camera configurations. The image from the left camera is shown in red and the image from the right camera is shown in cyan.

As previously described, stereo image pairs were captured using two cameras mounted to a rigid, horizontal flat plate located 1 *m* above the simulant bed. The stereo camera pair was calibrated using the Stereo Camera Calibrator app available as part of the MATLAB Computer Vision Toolbox, which uses a pinhole camera model that has been modified to account for lens distortions. The camera calibration produces the camera extrinsic and intrinsic parameters. The extrinsic parameters represent the location of the camera in the 3-D scene, while the intrinsic parameters represent the optical center and focal length of the camera. The calibration pattern used was a 9 by 6 checkerboard pattern with a checkerboard square size of 22 *mm*. The calibration pattern was attached to a rigid plate, and 25 images of this checkerboard pattern were captured by the stereo camera pair with the pattern at various locations within the cameras FOV. The mean reprojection error of the calibration, which is the average Euclidean distance between a checkerboard corner detected in a calibration image and a corresponding world point projected into the same image, was calculated to be 0.57 *px*.

The intrinsic and extrinsic parameters resulting from the camera calibration process were used to rectify each stereo image pair such that the epipolar lines between the two images were parallel [34, 46]. Since the epipolar lines were parallel, the search for common features between the images was limited along the same horizontal epipolar lines resulting in efficient image processing [47]. The disparity map was then calculated by matching the common features between the two image pairs using the semi-global method [35] available as part of the MATLAB Computer Vision Toolbox. The semi-global method [35] was selected over the more traditional block-matching method [48] as it was found to produce higher quality disparity maps for the highly textured simulant surface. This is likely due to the semi-global method making use of mutual information as a superior measure of local correspondence and the assumption that the disparity of neighboring pixels are likely to have the same or similar disparity [34]. As a result, the semi-global method is more robust against lighting and other variations between the stereo image pairs [34].

A uniqueness threshold value of 30 was used to remove potentially erroneous disparity measurements. The uniqueness threshold applies to the cost matching algorithm used for matching features between the stereo image pairs, and represents the difference required between the best match and the second best match for a disparity value to be

considered reliable [34]. Higher values of uniqueness threshold improve the signal to noise ratio at the expense of potentially removing valid data. The uniqueness threshold for this study was determined by testing values from 0, which applies no filtering, to 50, which was found to remove valid data. The resulting reconstructions were qualitatively analyzed for the tested values of uniqueness threshold, and a value of 30 was determined to be a good compromise between removing spurious measurements while minimizing the amount of valid data removed.

The resulting disparity values are inversely proportional to the depth of the target object at that pixel location and were therefore used to produce a three-dimensional reconstruction from the stereo image pair. This three-dimensional reconstruction is stored in the form of a *point cloud*, which is an N-by-3 array, where N is the number of points in the point cloud and the other 3 values represent the x, y, and z coordinates, respectively. The camera configuration used for this study resulted in a point cloud with a resolution of 36 $points/mm^2$. The resulting point cloud was then passed through a noise removal algorithm to remove outlier points. The outlier removal algorithm works by first calculating the mean distance from each point to its n_p-nearest neighbors as

$$\overline{X}_i = \frac{\sum_{j=1}^{n_p} X_{ij}}{n},\tag{1}$$

where $\overline{X}_i$ is the mean distance to n-nearest neighbors for point i, n_p is the number of nearest neighbors included in the search, and X_{ij} is the magnitude of the distance from point i to nearest neighbor j. For this work, 64 neighbors were used ($n_p = 64$) in the noise removal algorithm. Next, the mean of $\overline{X}$ was calculated as

$$\chi = \frac{\sum_{i=1}^{N} \overline{X}_i}{N},\tag{2}$$

where χ is the overall mean distance to n-nearest neighbors, and N is the total number of points in the point cloud. We can calculate the standard deviation of χ as

$$\sigma_\chi = \sqrt{\frac{\sum_{i=1}^{N}(\overline{X}_i - \chi)}{N}}.\tag{3}$$

Finally, a point is marked as an outlier and removed if $|\overline{X}_i - \chi| > \sigma_\chi$. An example point cloud is shown in Fig. 5, which shows the 3-D reconstructed crater at a time of 500 ms for one of the $70D$ tests illustrating the three-dimensional features of the crater. Note that the white regions without points seen in Fig. 5 are a result of the nozzle obscuring the view of the crater, which can be seen in the raw camera images shown in Fig. 3. Further details regarding the current stereo-photogrammetry process can be found in Refs. [34, 47]. From the 3-D reconstruction of the crater, the depth, radius, and volume of the crater geometry were extracted. The following section describes the method in which these characteristic quantities of the crater were extracted from the 3-D point cloud data.
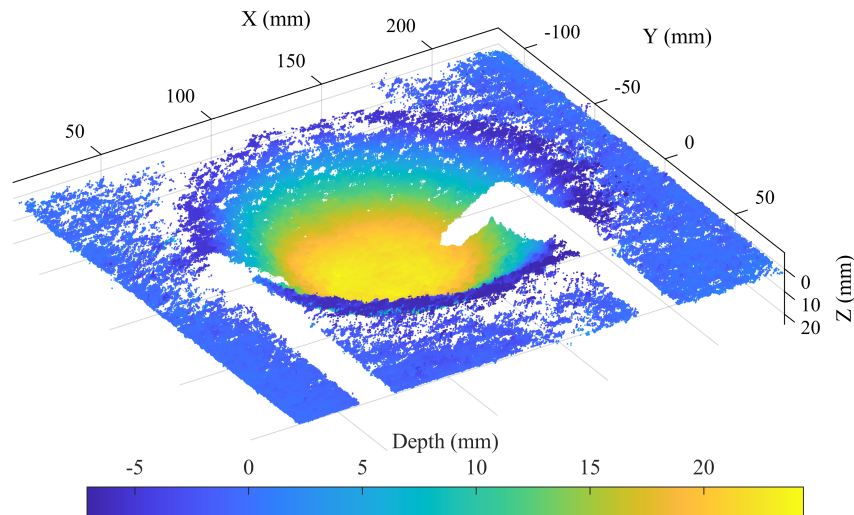

Fig. 5 A sample point cloud taken from one of the $70D$ **nozzle height tests at a time of** $500\ ms$**.**

B. Extraction of crater geometric parameters

The scene reconstruction yields points with their positions defined in a coordinate system originating at the left camera in the stereo camera pair. For data analysis, it was useful to re-cast the depth values of each point at each moment in time to instead be relative to the initial undisturbed simulant bed. The depth of the initial undisturbed simulant bed was obtained by fitting a two-dimensional planar surface function through the points on the 3-D reconstruction of the undisturbed simulant bed prior to initiation of the nozzle flow. This provided a local reference depth at any (x, y) location. Using a surface function to provide localized reference depths rather than using a single reference depth value for the entire simulant bed provides robustness against inaccuracies that would arise from the simulant bed not being totally flat and level prior to testing.

The crater formation process for this work was studied using three geometric parameters, i.e., crater depth, crater radius, and crater volume. The crater depth was defined as the depth of the deepest point in the crater measured relative to the height of the undisturbed simulant bed. The crater depth was calculated as the mean of the deepest point and its 100 nearest neighbors, which is given as,

$$\mu_{d,i}(t) = \frac{\sum_{j=1}^{n_p} d_j(t)}{n_p}, \tag{4}$$

where $\mu_{d,i}(t)$ is the mean depth for each experimental run, $d_j(t)$ is the depth of each point, and n_p (= 100) is the number of points considered to compute the average. The mean maximum depth was used to reduce susceptibility to noise and outlier points making the measurement more robust than if the single deepest point were used.

The crater radius was extracted from the computed 3-D crater geometry by taking a slice through the point cloud in the x-y plane to extract points within a 1 mm height range centered around the desired depth, z. This procedure resulted in a ring of points that represent the edge of the crater at that depth. Due to simulant particles ejected from the crater, optical access to the rim was limited, which made measuring radius at the rim unreliable. This issue was avoided by calculating the crater radius at a depth 5 mm below the original undisturbed surface, where the cameras had better optical access to the crater wall. Figure 6a shows an example of points extracted from a slice through the crater at a depth of 10 mm. Once these points were extracted, a circle was fit to these points using a least squares regression technique. Fitting a circle results in a single geometric parameter, the radius, to be extracted. Higher order fits, such as an elliptical fit, were tested and it was found that they were not necessary as the extracted crater slice was found to be circular. An example of the resulting fitted circle from this process is shown in Fig. 6b. Finally, the radius of the fitted circle, $\mu_{r,i}(t)$, was taken to represent the radius of the crater at the specified depth.
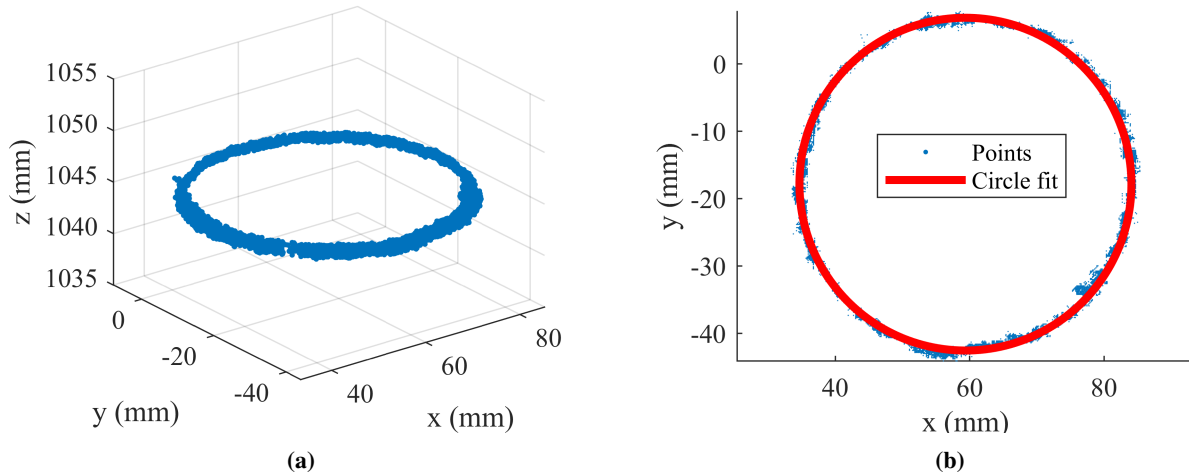

Fig. 6   Crater points extracted via slice at specified depth, (a) Isometric view, (b) Top down view with the circle fitted to the extracted points

The crater volume was determined from the point cloud using a numerical integration technique wherein the depth of each point in the crater was integrated over the surface area of the crater to result in the crater volume. However, since the 3-D point cloud data is a sparse unstructured format without any inherent information about which particles

are neighbors, a grid with uniform spacing of $\delta x = \delta y = 1\ mm$ in both the x and y directions was fit to the data before this integration could be performed. The grid was fit over a volumetric region of interest (ROI) of the point cloud qualitatively chosen to encompass the crater profile. The ROIs used had equal dimensions in the x and y direction chosen such that the maximum crater diameter would not exceed the ROI. The specific ROI dimensions in the x-y plane were 120 by 120 mm, 140 by 140 mm, 140 by 140 mm, and 220 by 220 mm for the $25D$, $40D$, $55D$, and $70D$ nozzle heights, respectively. In all cases, the ROI was centered on the crater with a top located at a depth of 2 mm below the surface of the sand bed, and a bottom extending to infinity. The ROI was set to start at a depth of 2 mm due to the low quality of the reconstruction at the crater rim resulting in a poor-quality mesh. The depth at each grid point was interpolated from the point cloud data using a cubic interpolation technique. The numerical integration was then performed over each point in the grid as

$$V(t) = \iint_S d(x, y, t)\, dS = \sum_{p=1}^{n_x} \sum_{q=1}^{n_y} d_{p,q}(t)\, \delta y\, \delta x, \tag{5}$$

where V is the volume of the crater, $d(x, y)$ is the depth of each grid point as a function of its location in the x-y plane, $dS = \delta x\, \delta y$ is the surface area of each grid cell, and n_x and n_y are the number of grid points in the x and y direction, respectively.

Three tests ($n_s = 3$) were conducted at each nozzle height to quantify the repeatability of the tests the and standard deviation across tests. The results at each nozzle height shown in the next section are calculated by averaging the extracted property, depth, radius, or volume, across each of the three tests at each time step as shown in Eq. 6, where $\mu_d(t)$ is the reported mean depth, $\mu_r(t)$ is the reported mean radius, $\mu_V(t)$ is the reported mean volume, $\mu_{d,i}(t)$ is the mean depth for each test, $\mu_{r,i}(t)$ is the mean radius for each test, $V_i(t)$ is the mean volume for each test, and n_s is the number of tests.

$$\mu_d(t) = \frac{\sum_{i=1}^{n_s} \mu_{d,i}(t)}{n_s}, \quad \mu_r(t) = \frac{\sum_{i=1}^{n_s} \mu_{r,i}(t)}{n_s}, \quad \mu_V(t) = \frac{\sum_{i=1}^{n_s} V_i(t)}{n_s} \tag{6}$$

The standard deviation of the data across the tests at each nozzle height is also calculated as shown in Eq. 7.

$$\sigma_d(t) = \sqrt{\frac{\sum_{i=1}^{n_s} \left(\mu_{d,i}(t) - \mu_d(t)^2\right)}{n_s}}, \quad \sigma_r(t) = \sqrt{\frac{\sum_{i=1}^{n_s} \left(\mu_{r,i}(t) - \mu_r(t)^2\right)}{n_s}}, \quad \sigma_V(t) = \sqrt{\frac{\sum_{i=1}^{n_s} \left(V_i(t) - \mu_V(t)^2\right)}{n_s}} \tag{7}$$

V. Results and Discussion

Experiments were conducted to quantify the accuracy of stereo-photogrammetry technique and apply the developed technique to obtain non-intrusive, three-dimensional measurements of the dynamic crater evolution process. The sections that follow present and discuss the results from these sets of experiments.

A. Stereo-Photogrammetry Accuracy

The accuracy of the current stereo-photogrammetry technique under ideal conditions was assessed by reconstructing objects with known dimensions. First, a 3-D calibration board using a dowel rod arrangement (schematic illustrated in Fig. 7a) was fabricated wherein, 25 dowel rods of variable lengths ranging from 4 mm to 118 mm were attached perpendicularly to a 3-D printed base. The dowel rods were placed in a grid arrangement with the spacing between each dowel rod maintained at 38.1 mm. The length of each of the dowel rods was then measured four times using a digital caliper with a precision of 0.01 mm. The mean of the four measurements was taken as the actual height of each dowel rod with the maximum standard deviation between the measurements observed to be 0.34 mm. Subsequently, stereo-photogrammetry was used to compute the 3-D reconstruction of the dowel rod arrangement. The height of each reconstructed dowel rod was compared with the actual height and the mean and standard deviation of their differences was observed to be 1.18 mm and 0.75 mm, respectively. From these results, it was concluded that depth measurements using the current technique are accurate to better than 2 mm under ideal conditions.

To further assess the accuracy of the depth, radius, and volume extraction techniques, measurements were obtained on a 3-D printed, parabolic "artificial" crater. A thin layer of sand ($600 - 850\ \mu m$) was affixed onto the artificial crater to better represent the actual simulant surface conditions. The resulting crater had a diameter of 101.6 mm and a depth of 50.8 mm, which is illustrated in Fig. 7b. The actual volume of the crater was measured by filling the

crater with water and measuring the net increase in weight of the 3-D printed crater. The actual depth and radius of the crater was measured using a digital caliper. After quantifying the geometric parameters of the artificial crater, stereo-photogrammetry was used to compute its 3-D reconstruction. The depth, radius, and volume were then extracted from the reconstructed point cloud using the methodology described in Section IV. The error between the actual and calculated depth, radius and the volume was 3.35%, 0.84% and 3.68%, respectively, which is summarized in Table 2.
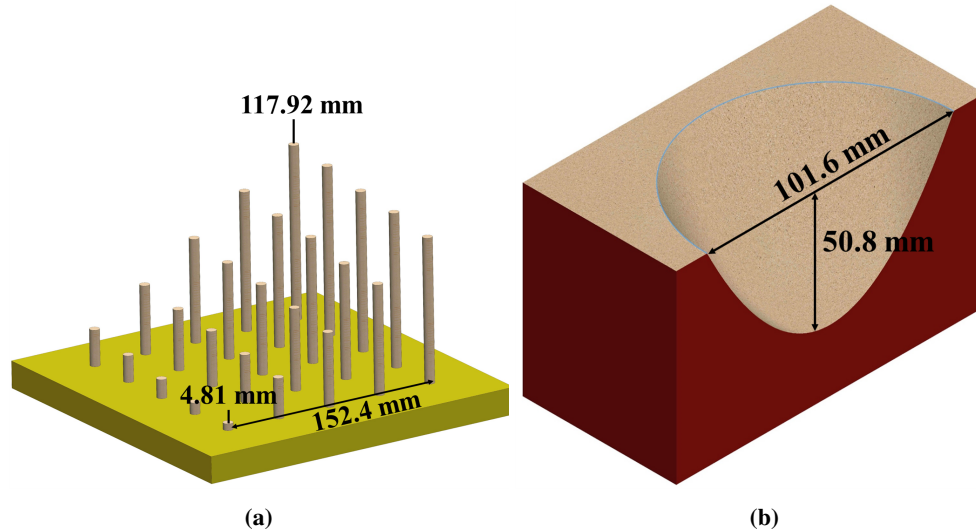
Fig. 7   (a) Dowel rod arrangement and (b) sectional view of the 3-D printed parabolic shaped crater for the accuracy assessment of the current stereo-photogrammetry technique.

Table 2   Actual and reconstructed values for depth, radius, and volume of the 3-D printed parabolic crater used to assess the accuracy of the stereo-photogrammetry technique.

Quantity	Actual	Measured via Photogrammetry	Absolute Error	% Error
Depth	50.8 *mm*	49.1 *mm*	1.7 *mm*	3.4
Radius 10 *mm* below rim	50.0 *mm*	49.6 *mm*	0.4 *mm*	0.8
Volume	200.0 *mL*	207.4 *mL*	7.4 *mL*	3.7

B. Effect of Nozzle Height on Crater Evolution Dynamics

This section presents the results of a series of tests conducted to apply the developed technique to measure the time evolution of the crater formation process in the full-domain experiment. First, a qualitative analysis of the crater cross-section evolution is presented. Then, the evolution of the crater depth, radius, and volume are quantified. Lastly, the crater formation mechanisms observed in the present study are discussed. For these tests, four different nozzle heights were selected, i.e., $70D$, $55D$, $40D$, and $25D$, where D is the nozzle exit diameter. Three tests ($n_s = 3$) were conducted at each nozzle height to verify the repeatability of the results and the nozzle flow was enabled for a duration of two seconds for all tests. The time history of the crater depth, radius and volume evolution was extracted from the 3-D crater geometry obtained using the stereo-photogrammetry technique as described in Sec. IV. The results at each nozzle height shown in this section were calculated by averaging the extracted property, depth, radius or volume, across the three experimental runs as shown in Eq. 6. The standard deviation of the data across the tests at each nozzle height was calculated as shown in Eq. 7 and is represented by the shaded region surrounding each line in the following plots.

For the results presented in this section, it is important to note that ejecta from the crater eventually obscured optical access to the crater for all but the $70D$ nozzle height case. For the nozzle height of $70D$, optical access to the crater was maintained throughout the test. However, for the lower nozzle height cases, the length of time that sufficient optical

access to the crater was maintained decreased with decreasing nozzle height. This is because the crater evolution process at lower nozzle heights is generally more rapid and energetic, resulting in a large amount of particulate being ejected from the crater obscuring the view of the cameras. Thus, for the $25D$, $40D$, and $55D$ nozzle heights, the depth, radius, and volume results were truncated at the point in time where the stereo processing algorithm began to fail.

1. Crater Depth

First, the time evolution of the crater cross-section taken through the center of the crater, shown in Fig. 8, was qualitatively analyzed for all nozzle heights tested. The cross-sectional view was generated by extracting points from the point cloud at a frontal plane that passes through the center of the crater. In this case, the crater center was taken to be the center of a circle fit to the points extracted from a depth-wise slice through the crater at a location of 5 mm above the bottom of the crater. The crater was observed to exhibit a parabolic profile for all nozzle heights, and the rate of increase in depth with time was observed to increase as nozzle height was decreased. Compared to the other cases, the depth-wise growth rate of the $25D$ case was very rapid, reaching a depth of 40 mm in 65 ms compared to the 250, 600, and 1, 000 ms for the $40D$, $55D$, and $70D$ cases, respectively. As discussed further in Sec. V.B.4, this rapid evolution indicates that bearing capacity failure [18, 22] may be the dominant formation mechanism for the $25D$ case, while viscous erosion [18] is likely the dominant mechanism for all other cases.
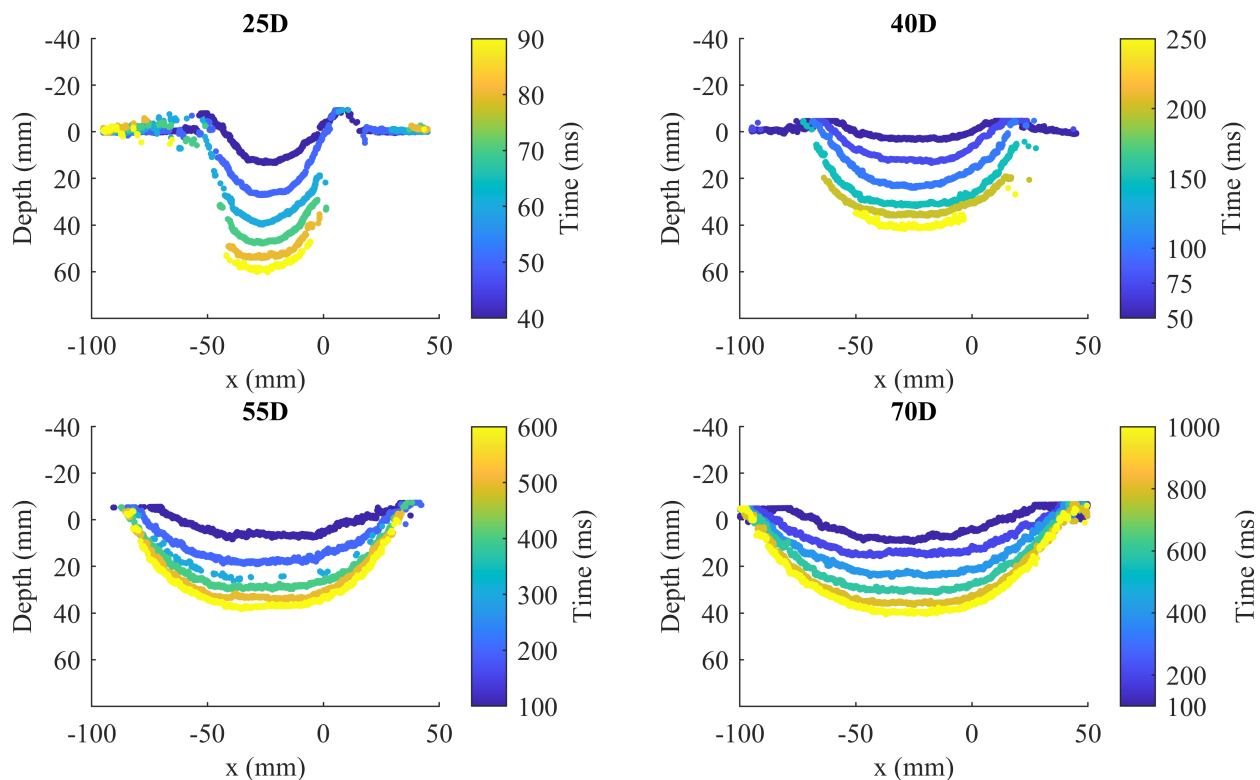

Fig. 8 **Cross-sectional view of the crater evolution over time for the four nozzle heights tested. Color denotes time progression and the specific time steps shown in each case are the labels on the colorbar.**

The temporal evolution of crater depth extracted from the measured 3D data, illustrated in Fig. 9, exhibited logarithmic growth over time. This logarithmic behaviour of the crater depth growth has been identified by previous studies in the case of viscous erosion, and a fit of the form $d(t) = a_1 \ln(b_1 t + 1)$ is commonly applied [18, 22]. In this case, the a_1 and b_1 coefficients can be viewed as the length and time scales, respectively [18]. This logarithmic fit applied to the depth evolution results is shown in Figs. 9a and 9b. The coefficients and the root mean squared error (RMSE) of the logarithmic fits are summarized in Table 3. The quality of the logarithmic depth fit is high for the $55D$ and $70D$ cases, which both have a RMSE of less than 1.2 mm. However, it was found that the quality of the fit was worse for the $25D$ and $40D$ cases, which had RMSE values of 6.90 mm and 3.55 mm, respectively.

An arctangent fit for crater depth evolution of the form $d(t) = a_2 \tan^{-1}(b_2(t^{c_2}))$, where a_2, b_2, and c_2 are fitting

parameters, was used by LaMarche and Curtis [22]. LaMarche and Curtis found the arctangent fit to be a better fit than the logarithmic fit in situations where the crater depth evolved rapidly towards an asymptotic value, such as in the case of bearing capacity failure, while still maintaining a good representation of craters that exhibit logarithmic depth growth [22]. This arctangent fit applied to the crater depth evolution data acquired in this study is shown in Figs. 9c and 9d. The fitting parameters and the RMSE are summarized in Table 3. Comparing the RMSE values between the arctangent and logarithmic fits, it was concluded that the arctangent fit was a better fit for the cases of 25D and 40D than the logarithmic fit due to the rapid depth evolution experienced in those cases. This further indicates that bearing capacity failure may play a significant role in these cases, whereas the 55D and 70D cases experienced the slower evolution expected of viscous erosion dominated crater formation. Further discussion on the crater formation mechanisms is presented in Sec. V.B.4.
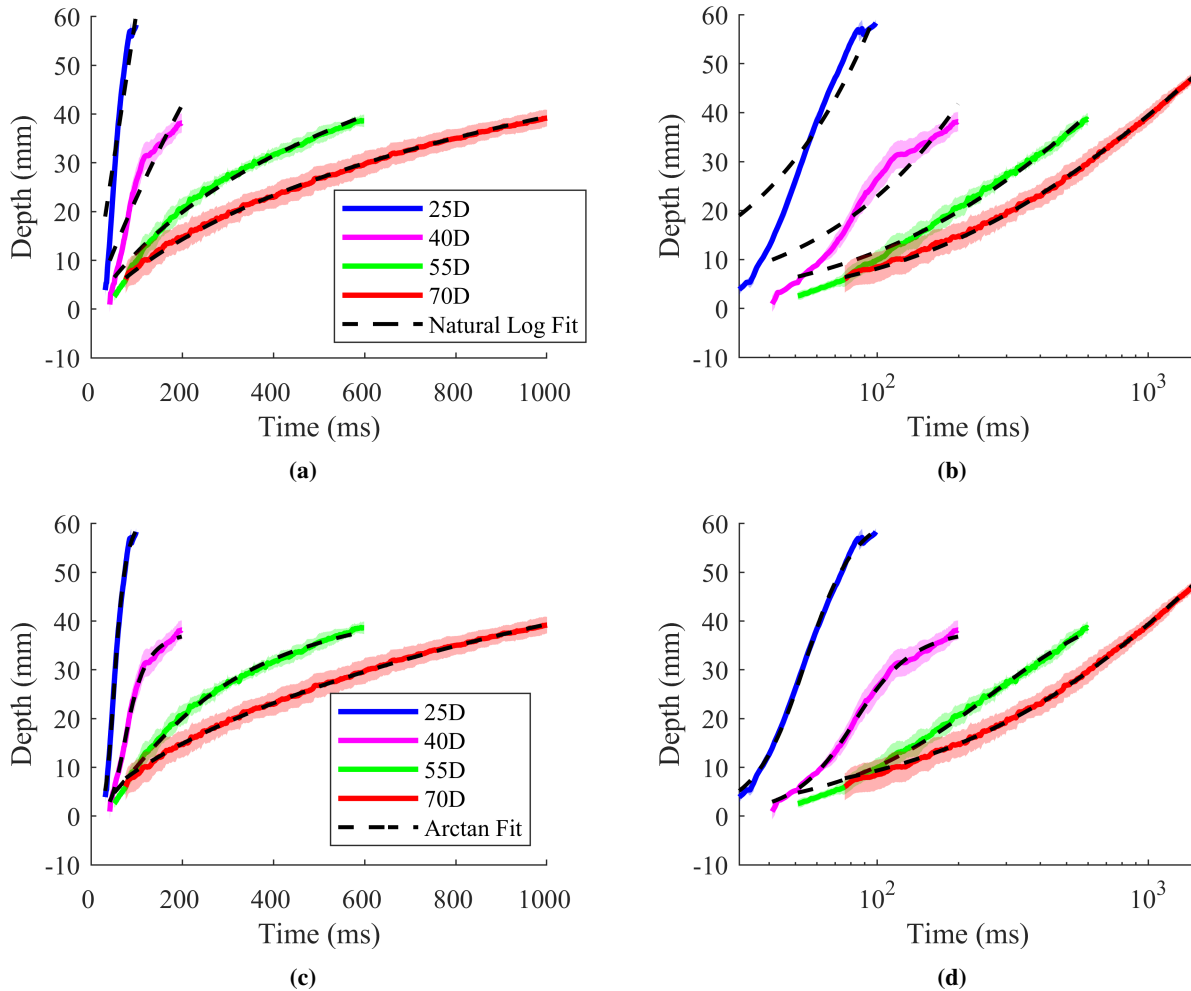

Fig. 9   Crater depth evolution over time for multiple nozzle heights on a linear (a) and (c) and logarithmic (b) and (d) scale. The solid line represents the mean (μ_d) and the shaded region represents the standard deviation (σ_d) over the three tests for each nozzle height. The dashed black lines show the logarithmic fit in (a) and (b) and the arctangent fit in (c) and (d).

Table 3 Coefficients and root mean squared error (RMSE) of the logarithmic and arctangent fit to the crater depth evolution data.

Nozzle Height (h/D)	a_1	b_1	RMSE Log Fit	a_2	b_2	c_2	RMSE Arctan Fit
25	6892.43	8.89×10^{-5}	6.90	40.18	4.89×10^{-7}	3.64	0.76
40	113.56	2.23×10^{-3}	3.55	24.51	1.50×10^{-6}	3.04	0.63
55	28.48	5.04×10^{-3}	1.10	31.34	1.68×10^{-3}	1.15	0.66
70	24.92	3.87×10^{-3}	0.33	63.43	6.40×10^{-3}	0.68	0.28

2. Crater Radius

The radius of the crater at a depth of 5 *mm* below the initial surface, shown in Fig. 10, was found to evolve rapidly for all nozzle heights before transitioning into a slower growth rate that appears to be approaching an asymptotic radius. The point where the radius evolution shifts from very rapid to slower evolution was found to occur at a radius value of $40 - 50$ *mm* for all nozzle heights. The crater radius for the $40D$, $55D$, and $70D$ cases appeared to be asymptotically approaching values of 45, 50, and 60 *mm*, respectively. Optical access to the crater for the $25D$ case was lost before this transition in crater growth rate could be observed, so it can not be concluded from the current data set if the $25D$ case would eventually show a similar transition in radius growth rate. The asymptotic radius value at a depth of 5 *mm* was found to increase with nozzle height, which is hypothesized to be a result of the jet at a depth of 5 *mm* becoming increasingly expanded as nozzle height increases. As the jet expands, the jet diameter of the jet increases, and is consequently able to support a larger crater radius.
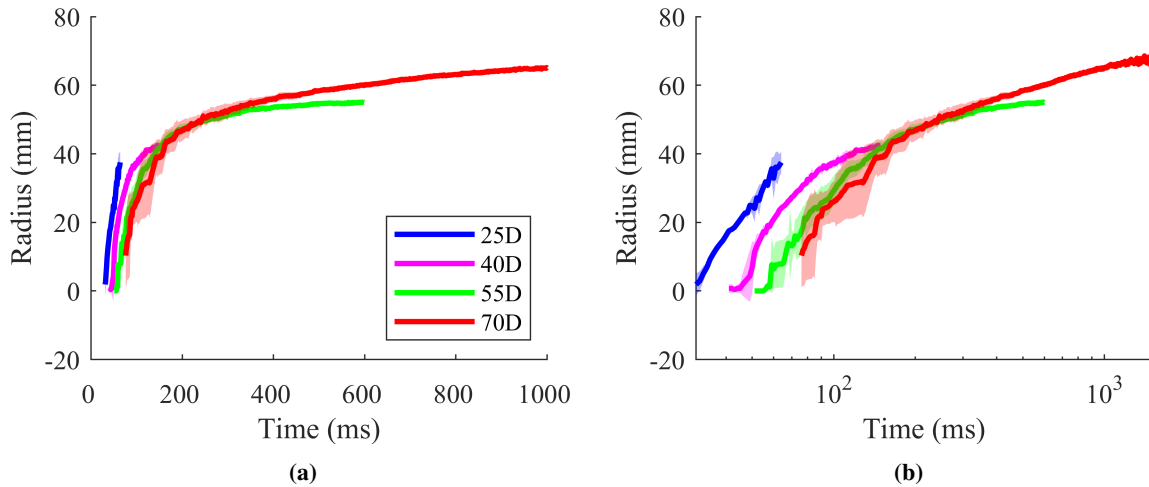

Fig. 10   Crater radius evolution over time for multiple nozzle heights on a linear (a) and logarithmic (b) scale. The solid line represents the mean (μ_r) and the shaded region representing the standard deviation (σ_r) over the three tests for each nozzle height.

Along with extracting the radius at a depth of 5 *mm*, the behavior of the crater radius was also investigated at depths of 15 *mm* and 10 *mm* below the initial surface. These results are shown for each nozzle height tested in Fig. 11. From these data, it is clear that the crater radius decreases throughout the depth of the crater with the crater being widest at the top and narrowest at the bottom. For the $40D$, $55D$, and $70D$ nozzle heights, the radius at each depth appears to grow very rapidly before then asymptotically approaching some steady value. The steady radius value is less at deeper locations within the crater, which is expected for parabolic shape craters. For the $25D$ case, optical access to the crater started to degrade around 50 *ms*, so conclusions about its asymptotic behavior cannot be made from the current data set.
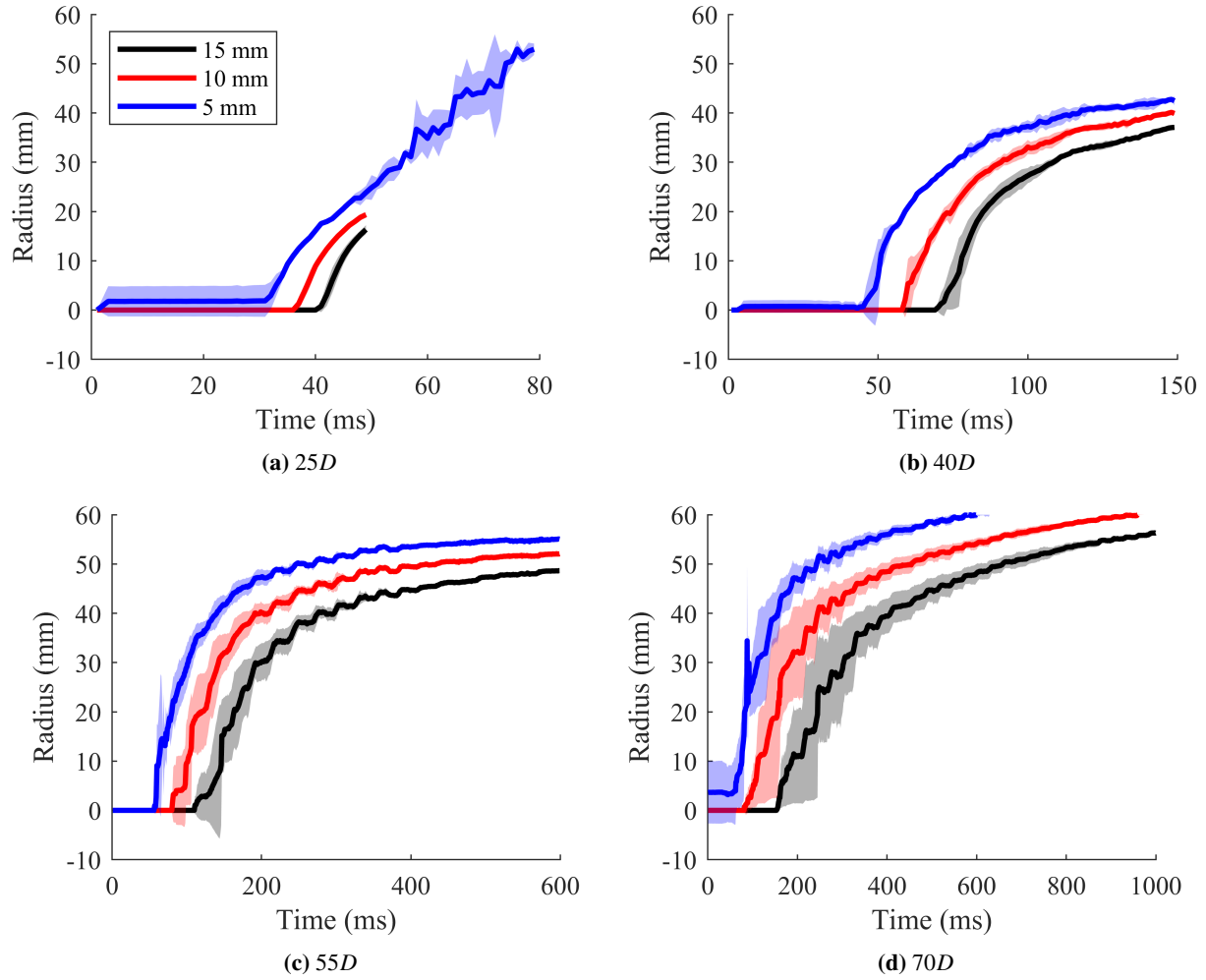
15

Fig. 11 **Radius evolution of the crater at** 10 *mm*, 5 *mm*, **and** 2 *mm* **below the initial surface height for the nozzle heights tested. The solid line represents the mean** (μ_r) **and the shaded region represents the standard deviation** (σ_r) **over the three tests for each nozzle height.**

3. Crater Volume

In addition to depth and radius, the volume evolution of the crater was calculated and is shown in Fig. 12. As the nozzle height reduces, the shear stress at the simulant bed is expected to increase resulting in increased erosion rate [30]. Such behavior is apparent from the data shown in Fig. 12, which show a higher rate of increase in crater volume over time as the nozzle height decreases. The volume growth for the 70*D* and 55*D* cases was found to be fairly similar whereas the volume growth for the 25*D* and 40*D* cases is notably more rapid. In contrast to the crater depth and radius, the crater volume evolution in the case of viscous erosion is best fit by a power law of the form $V(t) = \beta t^\alpha$ [18]. The power law fit is represented by the dashed black lines in Fig. 12 and the coefficients and quality of the power law fit are summarized in Table 4. The quality of the fit was found to be high with RMSE values of less than 4 *mL* for all cases except the 25*D* case, which had a significantly higher RMSE of 9.25 *mL*.

The power law fit is expected to fit the crater volume evolution data whenever the viscous erosion mechanism is dominant, i.e., in the latter stages of crater development. Therefore, it was necessary to extract the data during the time period that the viscous erosion mechanism was dominant. First, we estimated the time t_0 beyond which viscous erosion was assumed dominant for each nozzle height based on the moment in time that the erosion rate (presented in the next section) peaked and began to decay. Next, the volume V_0 at time t_0 was obtained, and the extracted data were shifted in time and volume so that the data at time t_0 were situated at the origin. The power law was then fit to the shifted data. Finally the values of t_0 and V_0 were used to shift the data back to its original position, and the power law curves were

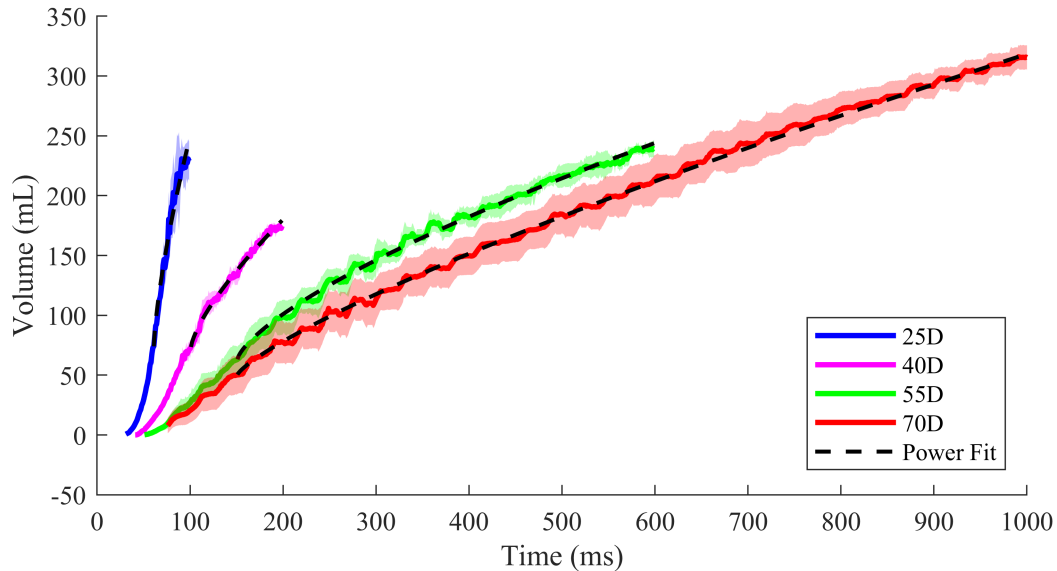superimposed on the volume vs. time data data as shown in Fig. 12.

Fig. 12 **Crater volume evolution over time for multiple nozzle heights. The solid line represents the mean (μ_V) and the shaded region representing the standard deviation (σ_V) over the three tests for each nozzle height. The dashed black lines show the power law fit.**

Table 4 **Coefficients and root mean squared error (RMSE) of the power law fit to the crater volume evolution data based on $V(t) = \beta t^\alpha$. The start time (t_0) for the power law fit is also shown.**

Nozzle Height (h/D)	β	α	RMSE	t_0 (ms)
25	12.62	0.72	9.25	60
40	3.67	0.73	2.76	100
55	2.41	0.71	3.24	150
70	1.26	0.79	3.41	150

4. Crater Formation Mechanisms

The crater evolution results for the 55D and 70D cases exhibit evolution behavior well characterized by expected trends of crater formation dominated by viscous erosion, while the 25D and 40D cases exhibit characteristics indicating bearing capacity failure may be occurring. As the nozzle height reduces, the stagnation pressure at the simulant surface increases. If the stagnation pressure exceeds the bearing capacity of the simulant, the bearing capacity failure crater formation mechanism dominates, and the simulant at the surface is pushed down creating a crater nearly cylindrical in shape with constant radius throughout its depth [18, 32]. From the data shown in Fig. 9a, the depth growth rate for the 25D and 40D cases appears nearly linear, suggesting that bearing capacity failure rather than viscous erosion may be the dominant mechanism in these cases. Furthermore, a notable change in slope of the depth evolution curve for the 40D case was seen at approximately 100 ms. This change in slope may indicate a transition between bearing capacity failure and viscous erosion modes as the depth of the crater increases, consequently increasing the effective distance between the bottom of the crater and the nozzle.

To further investigate the erosion mechanisms observed in the present study, the 3-D crater geometry data was analyzed to determine the distance between the location of maximum depth within the crater and the geometric center of the crater and is illustrated in Fig. 13a. In the case where crater formation is dominated by viscous erosion, Roberts'

theory of viscous erosion [26–29] states that the location of the maximum crater depth exists at some distance from the geometric center of the crater, which has been observed experimentally by Land and William [10]. This arises from the prediction that the maximum erosion occurs at the location of maximum dynamic pressure, which lies at some location radially displaced from the stagnation point at the center of the crater. From Fig. 13a, it was found that the location of maximum depth was at a finite distance away from the geometric center and that the distance from the maximum depth to the geometric center increased with nozzle height. This observation suggests that the crater formation process for the flow conditions in the current study was dominated by the viscous erosion process for the $40D$, $55D$, and $70D$ cases. However, it is important to note that Roberts' theory was developed for vacuum conditions where jet expansion is more significant compared to expansion under atmospheric conditions. Therefore, the distance from the point of maximum depth to the geometric center for the present study is expected to be less than the distance predicted by Roberts' theory. Furthermore, the peak at the geometric center of the crater is expected be less extreme due to the unsteady nature of the jet used in the present study increasing erosion at the nozzle centerline compared to the jets used in the development of Roberts' theory, which were non-turbulent at the centerline.

In the $25D$ nozzle height case, the distance from the geometric center to the location of maximum depth was found to be 2.4 mm, which is only marginally above the quantified error of the stereo-photogrammetry technique. This observation suggests that the location of the maximum dynamic pressure is very close to the center of the crater for this nozzle height, resulting in higher erosion at the crater center. This is further confirmed by the fact that the time-averaged crater radius extracted 5 mm above the bottom of the crater was lower for lower nozzle heights (Fig. 13b). As such, the possibility of bearing capacity failure cannot be neglected at lower nozzle heights, such as $25D$, where the stagnation pressure at the sand surface could exceed the bearing capacity of the sand. It is important to note, however, that the jet is less expanded at reduced nozzle heights, which could cause the maximum crater depth to form at locations very close to the crater center even without bearing capacity failure. While the results suggest that bearing capacity failure may be occurring at lower nozzle heights, the contribution of the reduced jet expansion cannot be neglected. Further studies are required to elucidate the dominating mechanisms for crater formation process at lower nozzle heights.
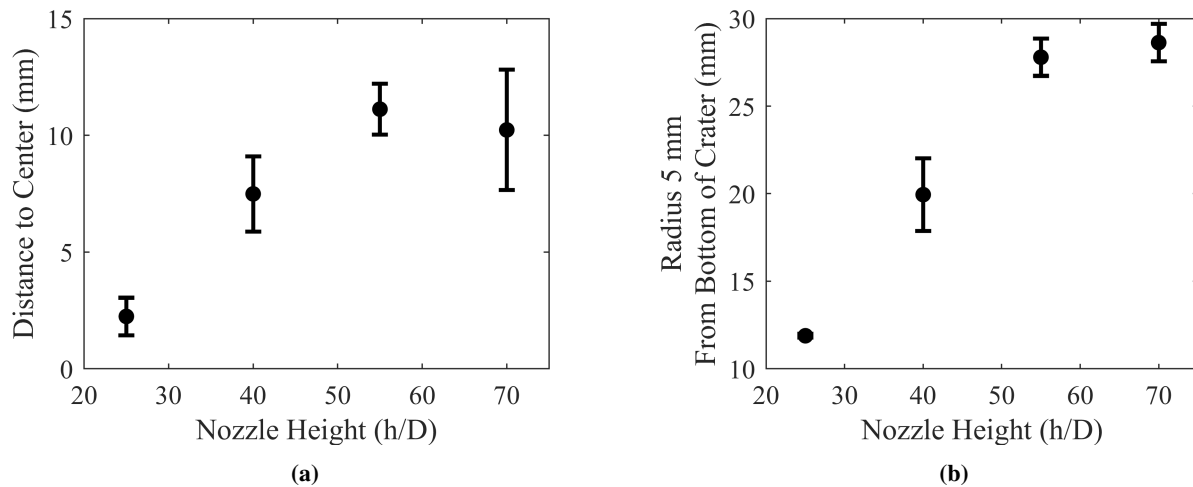

Fig. 13 **(a) Distance from the deepest point in the crater to the geometric center of the crater; (b) Time averaged crater radius at a depth of** 5 mm **above the crater depth. The markers represent the mean of the result across the three tests at each nozzle height and the error bars show the standard deviation.**

As a final investigation of the erosion mechanisms, the erosion rate $E(t) = dm/dt$ was calculated for both the experimental data as well as the power law fit and is shown in Fig. 14. The erosion rate for the experimental data was determined as the numerical derivative of the crater mass evolution, $\rho V(t)$, and the erosion rate derived from the power law is given by $E(t) = \rho(dV/dt) = \rho\alpha\beta t^{\alpha-1}$, where ρ is the bulk density of sand. The erosion rates for the $55D$ and $70D$ cases demonstrate an initial transient period before experiencing a region well characterized by the power law. For the $25D$ and $40D$ cases, the initial erosion rate rapidly rises to a value of nearly 10 kg/s and 3 kg/s, respectively. The decrease in erosion rate after the initial transient period is decently characterized by the power law for the $40D$ case, but the power law does not do a good job of characterizing the decrease in erosion rate of the $25D$ case. This serves as

further evidence that the crater formation in the $55D$ and $70D$ cases is dominated by viscous erosion, while the $25D$ and $40D$ cases may be experiencing bearing capacity failure and may not experience any viscous erosion period. As previously mentioned, the time period of useful data for the $25D$ and $40D$ cases was limited to $100\ ms$ and $200\ ms$, respectively, so the ultimate behavior of the erosion rate for these cases could not be determined.
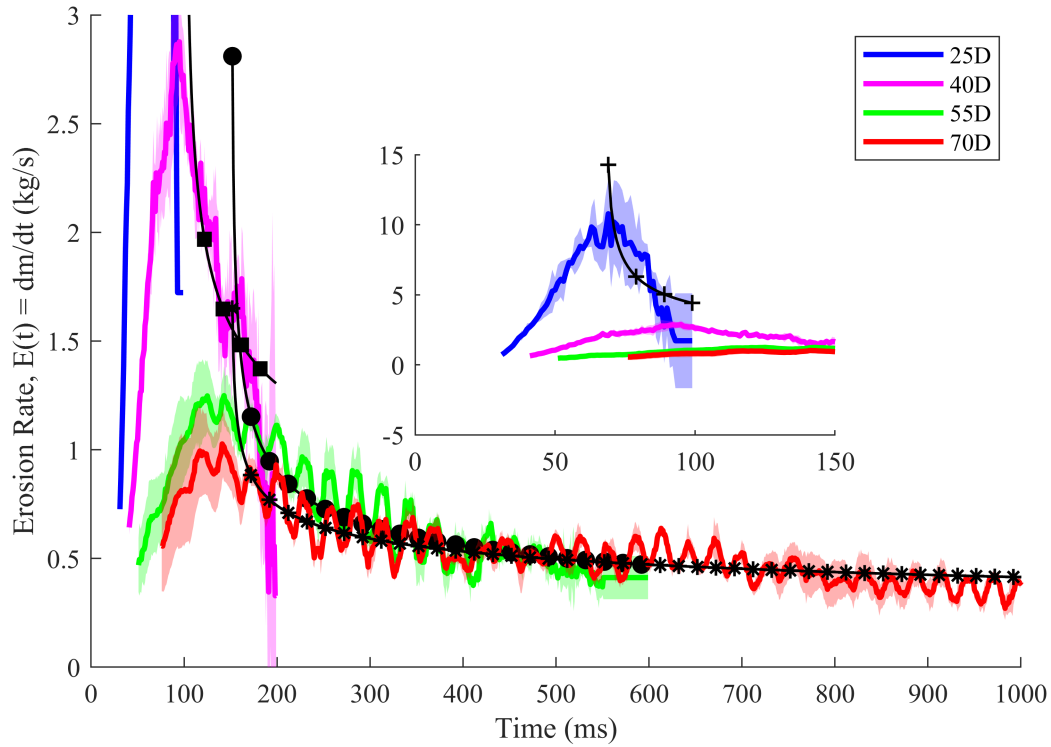

Fig. 14 Erosion rate of the crater over time for multiple nozzle heights. The solid colored line represents the mean (μ_E) and the shaded region represents the standard deviation (σ_E) over the three tests for each nozzle height. The solid black lines with plus, square, circle, or asterisk markers represent the derivative of the power law fit from the volume vs. time data for the $25D$, $40D$, $55D$, and $70D$ cases, respectively. The inset figure highlights the erosion rate behavior of the $25D$ case.

The results presented so far suggest that the developed methodology is able to successfully measure the dynamic crater evolution process up until the point that optical access to the crater is lost. The measurements obtained are in good agreement with expected crater behavior established in the literature, which serves as indication that the resulting crater measurements are accurate.

C. Crater Collapse After Nozzle Flow Shutoff

Since data were successfully extracted from the entire duration of the $70D$ nozzle height case, the crater collapse after the nozzle flow was stopped can also be examined. This behavior is not shown for the lower nozzle heights because optical access to the crater was blocked by the ejecta plume at that point in those cases. Figure 15 shows a time history of the crater depth, radius, and volume for the $70D$ case focusing on $t = 2\ s$ when nozzle flow was stopped. While flow from the nozzle is impinging upon the regolith surface, dynamic pressure and shear stress from the impinging flow allow the crater to maintain a slope steeper than the angle of repose of the simulant. However, once the flow is stopped, the forces holding the crater in shape cease. At this point, the crater shape is unstable and collapses to reach a new equilibrium in the absence of the fluid dynamics forces. The collapse process results in a rapid decrease in crater depth and volume with a less rapid increase in radius as simulant slides into the crater, which can be seen in Fig. 15. The crater radius was observed to decrease briefly before increasing again during the crater collapse process. While the data during this time period are noisy, a closer look at the data revealed that the momentary decrease in radius is physical. It is

speculated that the transients of the nozzle flow shutoff results in the crater losing the support of the fluid dynamic forces and collapsing from the top down. Future work will investigate this aspect of the crater collapse process in greater detail.
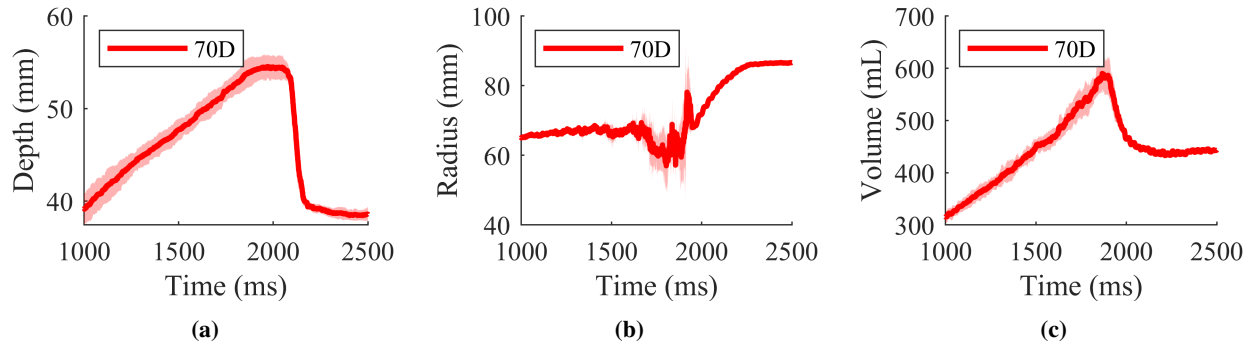

Fig. 15 Change in crater depth (a), radius (b), and volume (c) as the crater collapses after nozzle flow is stopped. The solid line and shaded region represent the mean and standard deviation of each reported property, respectively.
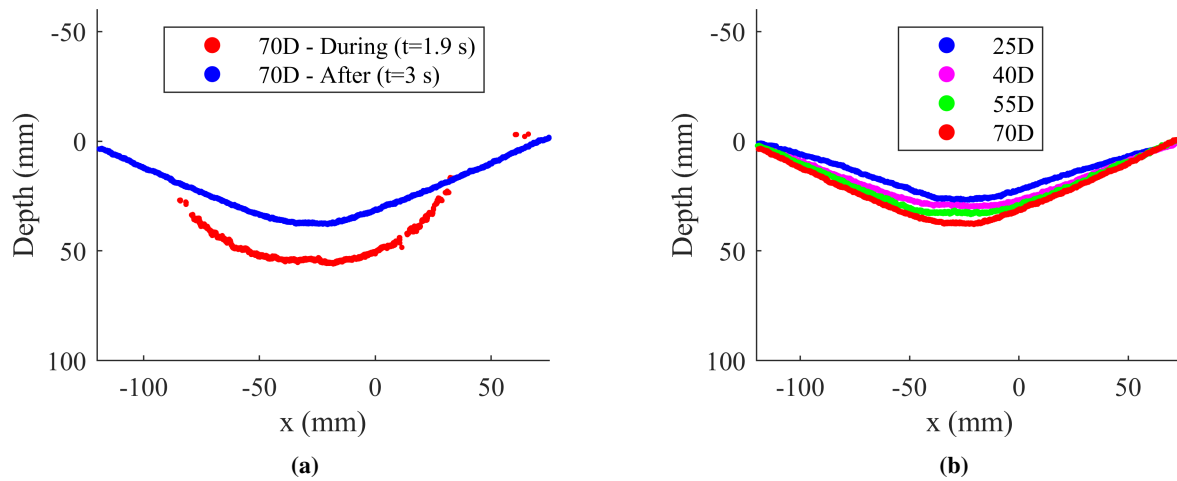

Fig. 16 (a) Comparison of a slice through the crater profile during and after nozzle flow for a nozzle height of $70D$ **demonstrating how the crater collapses after the flow is stopped. (b) Comparison of the 2-D crater profiles once the simulant reaches an equilibrium after the nozzle flow is stopped for multiple nozzle heights.**

The resulting post-collapse crater profile is shallower and wider than the pre-collapse crater. To further illustrate this behavior, Fig. 16a shows a slice through the center of the crater of the $70D$ nozzle height case with nozzle flow ($t = 1.9s$) and after the crater has reached a new equilibrium once the nozzle flow is stopped ($t = 3s$). The resulting slope of the collapsed crater walls is dominated by the dynamic friction coefficient of the simulant. Figure 16b shows the final crater profile for all of the nozzle heights tested. From these final crater profiles, the slope of the crater walls and the final crater volumes were calculated and are summarized in Table 5. It was found that the slope of the collapsed crater post nozzle flow increases with increasing nozzle height. This behavior is due to lower nozzle heights creating a crater with a steeper wall while the nozzle is flowing. The steeper crater wall results in a slope collapse having higher velocity and simulant momentum which ultimately results in a shallower crater post-collapse compared to higher nozzle heights. This behavior can also be seen in the final crater volume for the nozzle heights tested summarized in Table 5. Despite the lower nozzle heights having a more rapid crater growth rate, the final crater volume was found to increase with nozzle height. This is taken as further evidence that the crater collapse process is more violent for the lower nozzle heights and therefore the post-collapse crater volume for those nozzle heights is lower due to more simulant infilling the

crater during the collapse when the nozzle flow is stopped. It should be noted that the reason for crater volume not being the same pre- and post-collapse is likely due to the use of the volumetric ROI as described in Section IV.B. During the tests, sand was ejected outside of this ROI and therefore mass and consequently crater volume was not conserved. The measured decrease in crater volume is likely being compensated for by a change in height of the sand bed at a height above 2 *mm* and/or at a distance outside of the crater ROI. We expect that if the surface reconstruction was done for the entirety of the sand bed, then the volume would be the same before and after the collapse.

Table 5 Slope and volume of the collapsed crater after nozzle flow shutoff; data are presented as Mean ± Standard deviation

Nozzle Height (h/D)	Collapsed Crater Slope	Collapsed Crater Volume (*mL*)
25	14.1° ± 0.5°	272.5 ± 6.9
40	15.1° ± 0.1°	387.6 ± 13.5
55	16.3° ± 0.2°	409.9 ± 13.7
70	18.7° ± 0.3°	445.0 ± 1.9

VI. Conclusions

In this study, an atmospheric, full-domain, experimental facility was designed and constructed to facilitate non-intrusive measurements of the crater geometry during the PSI process. A supersonic impinging jet was used to simulate the exhaust of a descending rocket during the PSI process. Constant nozzle heights of $25D$, $40D$, $55D$, and $70D$ above the lunar regolith simulant bed were tested. Sand having a particle size range of 600 to 850 μm was used as the lunar regolith simulant. A pair of high-speed cameras was mounted above the simulant bed to allow for stereo imaging of the crater, and a methodology was developed to acquire time-resolved, full-domain, 3-D reconstructions of the crater geometry using stereo-photogrammetry. The accuracy of the method was assessed using a dowel rod board and 3-D printed crater geometries and was found to be on the order of 2 *mm* for the depth and radius measurements and on the order of 10 *mL* for the volume measurements.

The crater formation process was reconstructed in 3-D from the stereo image pairs. Crater depth, radius, and volume time histories were extracted from the 3-D crater reconstructions. The depth, radius, and volume growth rates were found to increase as the nozzle height decreased. The crater depth was observed to grow logarithmically for the $55D$ and $70D$ cases and exhibited much more rapid growth for the $25D$ and $40D$ cases. The crater volume growth rate was found to be well characterized by a power law fit. These logarithmic and power law fits have been used in previous works to characterize the expected crater growth behavior and are used here as a point of reference to demonstrate the success of the measurement methodology. The crater collapse post nozzle flow was also examined; it was found that once the surface pressure caused by the nozzle flow is removed, the crater collapses resulting in a rapid decrease in depth and volume, and an increase in radius. The slope of the collapsed crater post nozzle flow was calculated and found to increase with nozzle height along with the final volume of the post-collapse crater as a result of the crater slope prior to nozzle shutoff.

In summary, non-intrusive measurement techniques such as stereo-photogrammetry avoid the use of intrusive experimental setups that incorporate splitter plates that almost certainly affect experimental results. This study shows that the stereo-photogrammetry methodology implemented here successfully, accurately, and non-intrusively measures the full-domain crater evolution process as long as adequate optical access to the crater is maintained. Such non-intrusive measurements of the dynamic crater formation have not previously been reported in the literature to the best of the authors' knowledge. Additionally, early crater formation time measurements, i.e., less than 1 *s*, have not been reported by previous studies and are of particular interest for developing and validating codes to simulate the complex PSI process. Future work will focus on continuing to improve the performance of the method in optically degraded environments.

Acknowledgments

References

[1] Immer, C., Metzger, P., Hintze, P. E., Nick, A., and Horan, R., "Apollo 12 Lunar Module exhaust plume impingement on Lunar Surveyor III," *Icarus*, Vol. 211, No. 2, 2011, pp. 1089–1102. https://doi.org/10.1016/j.icarus.2010.11.013.

[2] Metzger, P. T., Lane, J. E., Immer, C. D., and Clements, S., "Cratering and blowing soil by rocket engines during lunar landings," *International Conference on Case Histories in Geotechnical Engineering*, 2008. URL https://scholarsmine.mst.edu/icchge/6icchge/session10/1.

[3] Gaier, J. R., "The effects of lunar dust on EVA systems during the Apollo missions," Tech. Rep. TM—2005-213610/REV1, NASA, 2007.

[4] Morris, A. B., Goldstein, D. B., Varghese, P. L., and Trafton, L. M., "Approach for Modeling Rocket Plume Impingement and Dust Dispersal on the Moon," *Journal of Spacecraft and Rockets*, Vol. 52, No. 2, 2015, pp. 362–374. https://doi.org/10.2514/1.A33058.

[5] Metzger, P. T., Smith, J., and Lane, J. E., "Phenomenology of soil erosion due to rocket exhaust on the Moon and the Mauna Kea lunar test site," *Journal of Geophysical Research: Planets*, Vol. 116, No. E6, 2011. https://doi.org/10.1029/2010JE003745.

[6] Metzger, P. T., "Rocket Exhaust Blowing Soil in Near Vacuum Conditions Is Faster than Predicted by Continuum Scaling Laws," *Earth and Space 2016: Engineering for Extreme Environments*, 2016, pp. 58–66. https://doi.org/10.1061/9780784479971.007.

[7] Eastman, D. W., and Radtke, L. P., "Flow field of an exhaust plume impinging on a simulated lunar surface," *AIAA Journal*, Vol. 1, No. 6, 1963, pp. 1430–1431. https://doi.org/10.2514/3.1819.

[8] Piesik, E. T., Koppang, R. R., and Simkin, D. J., "Rocket-exhaust impingement on a flat plate at high vacuum," *Journal of Spacecraft and Rockets*, Vol. 3, No. 11, 1966, pp. 1650–1657. https://doi.org/10.2514/3.28720.

[9] Clark, L. V., "Experimental Investigation of Close-Range Rocket-Exhaust Impingement on Surfaces in a Vacuum," Tech. Rep. TN-D-5895, NASA, 1970.

[10] Land, N. S., and Conner, D. W., "Laboratory Simulation of Lunar Surface Erosion by Rockets," *13th Annual Institute of Environmental Sciences Technical Meeting*, 1967.

[11] Rajaratnam, N., "Erosion by Submerged Circular Jets," *Journal of the Hydraulics Division*, Vol. 108, No. 2, 1982, pp. 262–267. https://doi.org/10.1061/JYCEAJ.0005821.

[12] Rajaratnam, N., and Beltaos, S., "Erosion by Impinging Circular Turbulent Jets," *Journal of the Hydraulics Division*, Vol. 103, No. 10, 1977, pp. 1191–1205. https://doi.org/10.1061/JYCEAJ.0004852.

[13] Rajaratnam, N., and Mazurek, K., "Erosion of a polystyrene bed by obliquely impinging circular turbulent air jets," *Journal of Hydraulic Research*, Vol. 40, No. 6, 2002, pp. 709–716. https://doi.org/10.1080/00221680209499917.

[14] Clark, A. H., and Behringer, R. P., "Jet-induced 2-D crater formation with horizontal symmetry breaking," *Granular Matter*, Vol. 16, No. 4, 2014, pp. 433–440. https://doi.org/10.1007/s10035-014-0501-9.

[15] Badr, S., Gauthier, G., and Gondret, P., "Crater jet morphology," *Physics of Fluids*, Vol. 28, No. 3, 2016, p. 033305. https://doi.org/10.1063/1.4943160.

[16] Haehnel, R. B., Cushman-Roisin, B., and Dade, W. B., "Cratering by a Subsonic Jet Impinging on a Bed of Loose Particles," *Earth & Space 2006*, 2006, pp. 1–8. https://doi.org/10.1061/40830(188)19.

[17] Haehnel, R. B., Dade, W. B., and Cushman-Roisin, B., "Crater Evolution Due to a Jet Impinging on a Bed of Loose Particles," *Earth & Space 2008*, 2008, pp. 1–10. https://doi.org/10.1061/40988(323)2.

[18] Metzger, P. T., Immer, C. D., Donahue, C. M., Vu, B. T., Latta, R. C., and Deyo-Svendsen, M., "Jet-Induced Cratering of a Granular Surface with Application to Lunar Spaceports," *Journal of Aerospace Engineering*, Vol. 22, No. 1, 2009, pp. 24–32. https://doi.org/10.1061/(ASCE)0893-1321(2009)22:1(24).

[19] Immer, C., and Metzger, P., "Rocket Cratering in Simulated Lunar and Martian Environments," *Earth and Space 2010: Engineering, Science, Construction, and Operations in Challenging Environments*, 2010, pp. 182–190. https://doi.org/10.1061/41096(366)20.

[20] Guleria, S. D., and Patil, D. V., "Experimental investigations of crater formation on granular bed subjected to an air-jet impingement," *Physics of Fluids*, Vol. 32, No. 5, 2020, p. 053309. https://doi.org/10.1063/5.0006613.

[21] LaMarche, C. Q., Curtis, J. S., and Metzger, P. T., "Cratering of a Lunar Soil Simulant, JSC-1A, by a Turbulent Subsonic Jet," *Earth and Space 2012: Engineering, Science, Construction, and Operations in Challenging Environments*, 2012, pp. 36–44. https://doi.org/10.1061/9780784412190.005.

[22] LaMarche, C. Q., and Curtis, J. S., "Cratering of a particle bed by a subsonic turbulent jet: Effect of particle shape, size and density," *Chemical Engineering Science*, Vol. 138, 2015, pp. 432–445. https://doi.org/10.1016/j.ces.2015.08.030.

[23] Metzger, P. T., Latta, R. C., Schuler, J. M., and Immer, C. D., "Craters Formed in Granular Beds by Impinging Jets of Gas," *AIP Conference Proceedings*, Vol. 1145, 2009, pp. 767–770. https://doi.org/10.1063/1.3180041.

[24] Mehta, M., Sengupta, A., Pokora, M., Hall, L., and Renno, N., "Mars Landing Engine Plume Impingement Ground Interaction," *Earth and Space 2010: Engineering, Science, Construction, and Operations in Challenging Environments*, 2010, pp. 143–157. https://doi.org/10.1061/41096(366)17.

[25] Mehta, M., Renno, N. O., Marshall, J., Rob Grover, M., Sengupta, A., Rusche, N. A., Kok, J. F., Arvidson, R. E., Markiewicz, W. J., Lemmon, M. T., and Smith, P. H., "Explosive erosion during the Phoenix landing exposes subsurface water on Mars," *Icarus*, Vol. 211, No. 1, 2011, pp. 172–194. https://doi.org/10.1016/j.icarus.2010.10.003.

[26] Roberts, L., "The interaction of a rocket exhaust with the lunar surface (Rocket exhaust jet interaction with lunar surface dust layer)," *Agard the Fluid Dyn. Aspects of space flight*, Vol. 2, 1966.

[27] Roberts, L., "The action of a hypersonic jet on a dust layer," *Institute of Aerospace Sciences 31st Annual Meeting*, 1963.

[28] Roberts, L., "Visibility and dust erosion during the lunar landing," *A compilation of recent research related to the Apollo Mission*, 1963, pp. 155–170.

[29] Roberts, L., "Exhaust Jet — Dust Layer Interaction During a Lunar Landing," *XIIIth International Astronautical Congress Varna 1962*, Springer, 1964, pp. 21–37. https://doi.org/10.1007/978-3-7091-4688-0_3.

[30] Hutton, R. E., "Comparison of soil erosion theory with scaled LM jet erosion tests," Tech. Rep. CR-66704, NASA, 1968.

[31] Metzger, P. T., Lane, J. E., and Immer, C. D., "Modification of Roberts' Theory for Rocket Exhaust Plumes Eroding Lunar Soil," *Earth & Space 2008: Engineering, Science, Construction, and Operations in Challenging Environments*, 2008, pp. 1–8. https://doi.org/10.1061/40988(323)4.

[32] Alexander, J., Roberds, W., and Scott, R., "Soil erosion by landing rockets," Tech. Rep. CR-65484, NASA, 1966.

[33] Scott, R. F., and Ko, H.-Y., "Transient rocket-engine gas flow in soil." *AIAA Journal*, Vol. 6, No. 2, 1968, pp. 258–264. https://doi.org/10.2514/3.4487.

[34] Kaehler, A., and Bradski, G., *Learning OpenCV 3: Computer Vision in C++ with the OpenCV Library*, O'Reilly Media, 2016.

[35] Hirschmuller, H., "Accurate and efficient stereo processing by semi-global matching and mutual information," *2005 IEEE Computer Society Conference on Computer Vision and Pattern Recognition (CVPR'05)*, Vol. 2, 2005, pp. 807–814 vol. 2. https://doi.org/10.1109/CVPR.2005.56.

[36] Burdziakowski, P., "UAV Design and Construction for Real Time Photogrammetry and Visual Navigation," *Proceedings - 2018 Baltic Geodetic Congress, BGC-Geomatics 2018*, Institute of Electrical and Electronics Engineers Inc., 2018, pp. 368–372. https://doi.org/10.1109/BGC-Geomatics.2018.00076.

[37] Griesbach, D., Baumbach, D., and Zuev, S., "Stereo-vision-aided inertial navigation for unknown indoor and outdoor environments," *IPIN 2014 - 2014 International Conference on Indoor Positioning and Indoor Navigation*, Institute of Electrical and Electronics Engineers Inc., 2014, pp. 709–716. https://doi.org/10.1109/IPIN.2014.7275548.

[38] Aguilar, M. A., Aguilar, F. J., and Negreiros, J., "Off-the-shelf laser scanning and close-range digital photogrammetry for measuring agricultural soils microrelief," *Biosystems Engineering*, Vol. 103, No. 4, 2009, pp. 504–517. https://doi.org/10.1016/j.biosystemseng.2009.02.010.

[39] Ouédraogo, M. M., Degré, A., Debouche, C., and Lisein, J., "The evaluation of unmanned aerial system-based photogrammetry and terrestrial laser scanning to generate DEMs of agricultural watersheds," *Geomorphology*, Vol. 214, 2014, pp. 339–355. https://doi.org/10.1016/j.geomorph.2014.02.016.

[40] Iglhaut, J., Cabo, C., Puliti, S., Piermattei, L., O'Connor, J., and Rosette, J., "Structure from Motion Photogrammetry in Forestry: a Review," *Current Forestry Reports*, Vol. 5, No. 3, 2019, pp. 155–168. https://doi.org/10.1007/s40725-019-00094-3.

[41] Harris, W. W., Viggiani, G., Mooney, M. A., and Finno, R. J., "Use of Stereophotogrammetry to Analyze the Development of Shear Bands in Sand," *Geotechnical Testing Journal*, Vol. 18, No. 4, 1995, pp. 405–420. https://doi.org/10.1520/GTJ11016J.

[42] Taconet, O., and Ciarletti, V., "Estimating soil roughness indices on a ridge-and-furrow surface using stereo photogrammetry," *Soil and Tillage Research*, Vol. 93, No. 1, 2007, pp. 64–76. https://doi.org/10.1016/j.still.2006.03.018.

[43] Tran, T. V., Tucker-Kulesza, S. E., and Bernhardt-Barry, M. L., "Determining Surface Roughness in Erosion Testing Using Digital Photogrammetry," *Geotechnical Testing Journal*, Vol. 40, No. 6, 2017, pp. 917–927. https://doi.org/10.1520/GTJ20160277.

[44] Kuang, S., LaMarche, C., Curtis, J., and Yu, A., "Discrete particle simulation of jet-induced cratering of a granular bed," *Powder Technology*, Vol. 239, 2013, pp. 319–336. https://doi.org/10.1016/j.powtec.2013.02.017.

[45] Raffel, M., "Background-oriented schlieren (BOS) techniques," *Experiments in Fluids*, Vol. 56, No. 3, 2015, p. 60. https://doi.org/10.1007/s00348-015-1927-5.

[46] Kumar, S., Micheloni, C., Piciarelli, C., and Foresti, G., "Stereo rectification of uncalibrated and heterogeneous images," *Pattern Recognition Letters*, Vol. 31, No. 11, 2010, pp. 1445–1452. https://doi.org/10.1016/j.patrec.2010.03.019.

[47] Kordelas, G. A., Alexiadis, D. S., Daras, P., and Izquierdo, E., "Enhanced disparity estimation in stereo images," *Image and Vision Computing*, Vol. 35, 2015, pp. 31–49. https://doi.org/10.1016/j.imavis.2014.12.001.

[48] Konolige, K., "Small Vision Systems: Hardware and Implementation," *Robotics Research*, edited by Y. Shirai and S. Hirose, Springer London, London, 1998, pp. 203–212. https://doi.org/10.1007/978-1-4471-1580-9_19.